

---

Theses and Dissertations

---

Fall 2010

## Airway segmentation of the ex-vivo mouse lung volume using voxel based classification

Tarunashree Yavarna  
*University of Iowa*

Follow this and additional works at: <https://ir.uiowa.edu/etd>



Part of the [Biomedical Engineering and Bioengineering Commons](#)

Copyright 2010 Tarunashree Yavarna

This thesis is available at Iowa Research Online: <https://ir.uiowa.edu/etd/909>

---

### Recommended Citation

Yavarna, Tarunashree. "Airway segmentation of the ex-vivo mouse lung volume using voxel based classification." MS (Master of Science) thesis, University of Iowa, 2010.  
<https://doi.org/10.17077/etd.gxc7wnyp>

---

Follow this and additional works at: <https://ir.uiowa.edu/etd>



Part of the [Biomedical Engineering and Bioengineering Commons](#)

AIRWAY SEGMENTATION OF THE EX-VIVO MOUSE LUNG VOLUME USING  
VOXEL BASED CLASSIFICATION

by  
Tarunashree Yavarna

A thesis submitted in partial fulfillment  
of the requirements for the Master of  
Science degree in Biomedical Engineering  
in the Graduate College of  
The University of Iowa

December 2010

Thesis Supervisor: Professor Joseph M.Reinhardt

Graduate College  
The University of Iowa  
Iowa City, Iowa

CERTIFICATE OF APPROVAL

---

MASTER'S THESIS

---

This is to certify that the Master's thesis of

Tarunashree Yavarna

has been approved by the Examining Committee  
for the thesis requirement for the Master of Science  
degree in Biomedical Engineering at the December 2010 graduation.

Thesis Committee: \_\_\_\_\_  
Joseph M.Reinhardt, Thesis Supervisor

\_\_\_\_\_  
Edwin L. Dove

\_\_\_\_\_  
Gary E. Christensen

To my family who offered me unconditional love and support throughout the course of this thesis.

## ACKNOWLEDGMENTS

In presenting this work of a two year long research I would first and above all like to express my sincere gratitude to my Advisor, Dr. Joseph M. Reinhardt, for guiding me through the expanse of this field and unconditionally supporting me as I developed my ideas. His rich experience and a friendly smile encouraged me to get through the most difficult times in my research so that I could progress faster and better in my project. As a student struggling through the trivia of everyday life in a University town, I cannot but thank him for ensuring my financial support through the NIH grants. I would also like to thank Prof Gary E. Christensen and Prof Edwin L. Dove for their support and guidance on the thesis. I must sincerely thank Dragos for his generous help in providing me with the data that fed integrally into my research. It is impossible to forget the contribution of all the faculty and staff at the University of Iowa who made my intellectual journey enjoyable and enriching.

In this long period, I could function emotionally due only to the unconditional love of my parents, my brother and sister-in-law, and my good friends Rahul, Katha, Shuhita, Vinayak and Abhilash. Every day at work was lit up unfailingly by the cheer and grace of my lab-mates who made the most trying times seem transitory. I had the most productive and enjoyable time with my lab mates, Xiayu Xu, Panfang Hua, Kaifang Du, Kai Ding and Sandeep, and would like to thank them all.

## TABLE OF CONTENTS

LIST OF TABLES .....	vi
LIST OF FIGURES .....	vii
CHAPTER	
I. INTRODUCTION .....	1
1.1 Motivation.....	1
II. BACKGROUND AND SIGNIFICANCE .....	3
2.1 Pulmonary anatomy and physiology of the mouse lung.....	3
2.2 Mouse Models for the Pulmonary Disease of Humans .....	4
2.3 Image Acquisition using Micro-Computed Tomography (Micro-CT) .....	5
2.5 Previous Work .....	6
2.6 Significance and Innovation of the work.....	9
III. METHODOLOGY .....	11
3.1 Overview.....	11
3.2 Feature Calculation .....	12
1. Convolution with Gaussian.....	14
2. First Order Derivative .....	16
3. Gradient Magnitude .....	16
4. Second Order Derivative .....	16
5. Laplacian.....	17
6. Eigen Values of Hessian.....	17
7. Gaussian Curvature.....	19
8. Eigen Magnitude.....	20
9. Ratios of Eigen Values .....	20
3.3 Training Sample Selection.....	22
3.4 Feature Selection .....	23
3.5 KNN- Classification .....	26
3.6 Implementation details.....	29
IV. RESULTS .....	32
4.1 Feature Calculation Results .....	32
4.2 Results for the Selection of the Best Suited Features .....	38
4.3 KNN Classification Results.....	39
V. DISCUSSION .....	47
5.1 Advantages of the proposed method.....	47
5.2 Factors influencing the Results.....	48
VI. CONCLUSION.....	51

REFERENCES .....	52
APPENDIX.....	55

## LIST OF TABLES

### Table

1. The set of 21 features calculated at 7 scales with corresponding equations .....	15
2. The Eigen values of the representing the possible patterns in the 3D image .....	19
3. Features selected during the feature selection method with their corresponding criterion value .....	40
4. Change in the specificity and sensitivity values across four threshold ranges .....	40
A1. Representation of the scale with the corresponding scale numbers .....	55
A2. Representation of the feature types with their corresponding feature numbers .....	56



## LIST OF FIGURES

### Figure

1. Gross Anatomy of mouse lung .....	3
2. Siemens Imtek Micro-CAT II scanner.....	5
3. Comparison between the ex-vivo and in-vivo scans (a) Ex-vivo micro-CT scan, (b) In-vivo micro- CT scan, with airway segmentation (c) Volume rendered ex- vivo segmented tree (d) Volume rendered ex-vivo segmented tree .....	10
4. Overview of the method.....	13
5. Gaussian distribution with mean 0 and Standard Deviation.....	18
6. Second order ellipsoid describing the local principal directions of curvature .....	23
7. Mid-slice sample selection of Airway and Non-airway voxel.....	24
8. Sequential forward floating search process (f1, f2 ...f147 – feature values and B1, B2, B3 – best features selected in the previous iteration) .....	27
9. Flow chart of selecting the set of best features by the Feature Selection method .....	28
10. X-Y scatter plot of a 2 dimensional feature space with 23 samples for KNN- classification (k = 4). .....	31
11. Flow chart of obtaining probability image from the KNN classifier.....	38
12. The set of 21 local image descriptors (feature images) calculated at scale 1 .....	39
13. Graph showing the criterion value achieved with the increase in the number of features selected.....	41
14. Graph showing the increase in the criterion value with changing number of training points .....	42
15. Probability images at 4 different thresholds of 0.2, 0.4, 0.6, and 0.8.....	43
16. Graph showing the area under the ROC curve from four different threshold values .....	45
17. Volume rendered airway segmentation for three different scans .....	46
18. Graph showing the increase in time per query point with the increase in the number of features (increase in dimension of feature space).....	46
19. Graph showing the reduction in the time of classification to classify all the voxels in a query image by increasing the error bound limits .....	49

20. Graph showing the change in the ROC curve with the changing error bound limits. ....	49
21. Volume rendering of an incorrectly segmented vessel running parallel to the airway wall, red arrow shows the vessel.....	50
22. Midslice of the scan showing the wall between the airway and the vessel. ....	50
23. Misclassification/Leakage of airways due to the incorrect threshold selection by the user .....	51

## CHAPTER 1 INTRODUCTION

### 1.1 Motivation

The spread of the pulmonary disease among humans is a very rapid process and it stands as the third highest killer in the United States of America. It is primarily caused by narrowing or blocking the airways which subjects patients to increasing difficulties in exhaling and getting sufficient oxygen supply. Statistically, among the lung diseases, chronic obstructive pulmonary disease (COPD) and asthma are reported as the most notorious ones with nearly 14.5 million Americans diagnosed with COPD [1] and 34.1 million Americans with asthma [2]. COPD comprises of chronic bronchitis (in which the bronchial tubes get scarred and inflamed) and emphysema (in which particular airways and air sacs get stretched out and lose their natural shape). An asthma attack causes the swelling of the airway lining and contraction of the muscle surrounding the bronchi leading to the narrowing of the airway. Therefore, pulmonary diseases resulting from the dysfunctioning of airways highlight the urgent necessity of analyzing airways for efficient diagnosis.

In today's world of biomedical technology, advanced imaging techniques have emerged as indispensable for the diagnosis of these varieties of pulmonary disease, following which therapeutic drugs can be administered to the patient. Clinical assessment of the lung function has been significantly enhanced by measuring the effect of drugs and infectious agents on different lung models of diseased mice. Our current technological sophistication enables us to measure these precise indices of lung function leading to important insights into the mechanisms of lung disease.

Computed tomography (CT) scanning allows us to obtain detailed images of the pulmonary anatomy including the airways. Airway lumen in the CT images can then be

identified through airway tree segmentation which can be performed manually by an image analyst. However, the complexity of the tree makes the process of manual segmentation tedious, time-consuming, and variant across individuals. In contrast, computer aided processing and analyzing of CT images enables an accurate segmentation of the airway tree. But computer aided processing introduces a different set of challenges stemming from image noise, ‘partial volume effect’, and texture similarity of the airway and parenchyma [3]. The resultant airway segmentation, whether arrived at manually or through the aid of computers, can then be used to measure airway geometry, study airway reactivity, and guide surgical interventions.

The thesis addresses these problems and suggests a fully automated technique for segmenting the airway tree in three-dimensional (3-D) micro-CT images of the thorax of an ex-vivo mouse. This novel technique is a several step approach consisting of:

1. The feature calculation of individual voxels of the micro-CT image,
2. Selection of the best features for classification (from step 1.),
3. K-nearest neighbor (KNN) classification of voxels by the best selected features (from step 2.) and
4. Region growing segmentation of the KNN classified probability image.

KNN classification algorithm has been used for the classification of the voxels of the image (into airway and non-airway voxels) based on the image features, the results of which have then been processed using the region growing segmentation algorithm to obtain the final set of results for segmentation. The segmented airway of the ex-vivo mouse lung volume is analyzed using a commercial software package to obtain the measurements. The following chapter will go on to explain the use of micro CT imaging and ex-vivo airway segmentation of the mouse lung as deployed in the course of the current research.

## CHAPTER 2

### BACKGROUND AND SIGNIFICANCE

#### 2.1 Pulmonary anatomy and physiology of the mouse lung

The lung is an important organ responsible for the gaseous exchange of air which circulates in and out of the body. The mouse lung can be divided into the right and left lungs which can then be further subdivided into four lobes in the right lung (Apical lobe, Azygous lobe, Cardiac lobe and Diaphragmatic lobe) and a single lobe in the left lung (Left lobe) as shown in figure 1. The total lung capacity of the mouse has been reported as 1ml [27]. In the mouse, 18% of the lung is comprised of parenchymal tissue while 11% is composed of airway [5]. The overall anatomy of the airway has a monopodial pattern with very few generations (13-17) and a relatively larger lumen at the base of the lung compared to the humans.

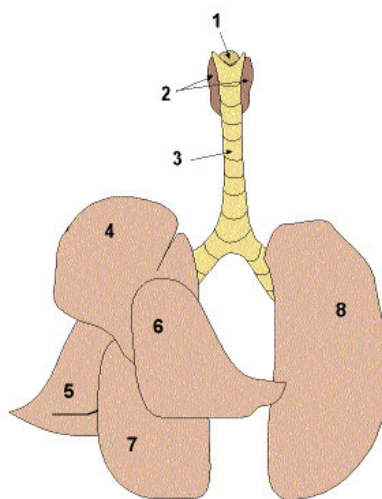


Figure 1. Gross Anatomy of mouse lung

1. Larynx, 2. Thyroids, 3. Trachea, 4. Apical Lobe, 5. Azygous Lobe, 6. Cardiac Lobe, 7. Diaphragmatic Lobe, 8. Left lobe. This figure is from [27].

The lung functioning is greatly aided by its architecture that consists of the airway tree serving as conduits of air. Both the sides of the lung have side bronchi projecting off from the main bronchi in three rows: Ventral row – consist of the longest branches and runs into the ventral periphery of the lungs, Dorsal row – which has smaller branches that supplies lung tissue adjacent to the vertebral column, and the Medial row which feeds the lung directed toward the posterior region of the mediastinum [6].

## 2.2 Mouse Models for Pulmonary Disease of Humans

Human Pulmonary Disease research has been greatly boosted by the enormous volume of information obtained from the genes of the mouse. This deeper research of the human diseased lung has been made possible by the use of mouse models to investigate and study the genetic basis of the disease.

Mouse models that mimic human disease play a vital role in understanding the cause and origin of cancer. For example, mouse models have been used to investigate agents that cause Human Melanoma and Lung Cancer [28]. Mice are the most widely used model for pulmonary research due to its close resemblance to the human lung physiologically and genetically. Also, they can be easily studied, understood and defined genetically. They also respond and develop pulmonary diseases in a manner very similar to human beings. Apart from being genetically similar to humans, the mouse is inexpensive to procure, and can be easily housed. Moreover, their age, sex and environmental factors can be easily controlled (unlike in the case of humans), and their quick supply readily ensured (because of their have short gestation periods which allows multiple generations to be acquired in a short period of time) [7]. Therefore, mouse is genetically the best characterized of all mammals.

### 2.3 Image Acquisition using Micro-Computed Tomography (Micro-CT)

Micro CT is a technique used to produce high resolution datasets using x-rays through a minimally invasive system for the screening of small animals. The imaging of an ex-vivo mouse lung volume using Micro-CT eliminates the problem of motion artifacts, thus allowing detailed fixed lung investigation. Fixed lung Micro-CT imaging enables early detection of lung diseases and also helps record the effect of drugs through a longitudinal study. This is made possible through the reduction of focal spot size (by decreasing the X-ray output power) and the increase of the signal to noise ratio (by increasing the exposure time). This technique is particularly helpful in the case of small animals. The radio density image information obtained from Micro-CT adds to the understanding of the physiological measures by usual methods for assessing physiology.



Figure 2. Siemens Intek Micro-CAT II scanner

During the image acquisition, X-rays pass through the small animal being imaged. MicroCAT II® (Siemens Preclinical Solutions) Micro-Computed Tomography Scanner is a state-of-the-art tool for investigating morphology and physiology in living small laboratory animals (up to 7 cm in diameter). This equipment allows non-invasive high-resolution (down to 27 microns) imaging of the same living animal over time to perform lateral studies, such as to monitor the progression of disease or the response to therapy.

## 2.5 Previous Work

There have been many methods proposed for the automatic segmentation of the human airway tree. Some of the previous work in segmenting the human airways from CT scans includes the algorithms of fuzzy connectivity, region growing methods, mathematical morphology methods and hybrid methods (region growing and mathematical morphology). The implementation of fuzzy logic method [8] for airway-tree detection increased the specificity of detection without compromising its sensitivity. However, the method was susceptible to movement artifacts and variety of changes in the pathological responses in the lung function. Another segmentation method performed using the algorithm of grayscale morphology [3] segments the airway tree on 2D slices which can then be reconstructed into a connected 3-D airway tree. This additional reconstruction proved the method to be less sensitive to detect in-plane branches. Also, this algorithm is greatly influenced by the selection of morphological parameters like endpoints in larger and smaller airways.

The human airway segmentation algorithm is most commonly done by the region growing approach but they often suffer leakages and/or disconnection due to the constant parameters used. This problem was solved by the segmenting the airways in an adaptive region growing approach [9].



In contrast to the above methods of image segmentation, there has been a significant amount of work put into finding the region of interest based on the pixel classification. For example, Loog et al. [23] proposed a method to reclassify every pixel of an initial segmentation on the original features and contextual information (class labels of the neighboring pixels). Another work done in the field of Ophthalmology by Merikel [24] et al. was to segment the optic disc based on the combination of graph search and pixel classification method. In this method, the pixel classification generated the probability image whose probability is maximized by a cost function of the graph search algorithm. A most recent work by Xu [25] detected the optic disc and fovea simultaneously by using their mutual information and k-nearest neighbor regression. Voxel classification method has also been applied in the segmentation of periprosthetic tissues in the CT scans [26]. This is one of the first automatic algorithms developed to segment the tissues correctly in spite of the low densities, metal induces artifacts and inter-patient and inter-scan variation.

In this context of segmenting the region of interest based on image intensities, Lo et al. [12] proposed a voxel based classification method for segmenting the airway tree of human lung using a complex appearance model. This algorithm is based on a set of local image appearance features and K- nearest neighbor classification. This framework for the segmentation of human airway tree is most relevant to the present work which has been extended to perform on excised mouse lung volume micro-CT images.

Therefore, the direct translation of the human airway tree segmentation algorithms cannot be done to mice micro-CT images because of the poor image quality of the image and complexity of the airway tree structure. There have been two recent algorithms developed for the automatic segmentation of airways from the in-vivo mice micro-CT scans.

The most recent work of Shi et al. [10] aims at segmenting the airways of an in-vivo mouse lung volume scan using the gray-scale morphology property of the images.

This algorithm segments the airways lumen in 2D transversal slices which are then used to reconstruct the full 3D tree. It uses a 3 step approach. In the first step of preprocessing, the image containing only the lung region is extracted and closed-space dilation performed. In the second step of morphology based 2D segmentation, each slice goes through image processing stages of noise removal, local minimum region detection and region filtering. In the last step, the 2D segmented slices are reconstructed into a 3D tree by connected region growing. The major drawback of this segmentation method was that it is primarily dependent on a 2D segmentation which may lead to problems due to the high variability of the shape of the airway lumens as seen in transversal slices. This algorithm also requires a lot of human intervention in cases of noisy images.

Another recent work of Artaechevarria et al. [11] uses a fast marching wave front propagation that grows and divides into tree segments in an in-vivo mouse lung volume scan. This algorithm is based on several rules to guarantee that the wave front propagates only inside the airway region and does not leak to the lung parenchyma. It not only segments the airway tree but also provides a reconstruction of the bronchial tree, by means of a list of hierarchically related segments. This algorithm is tested on normal and diseased mice and shows high sensitivity and specificity values. Although, this method detected the airways efficiently in minimal time, it was highly sensitive to image resolution, motion artifacts and signal-to-noise ratio. Also, any interruption in the propagation of wave due to image noise could not be detected leading to missing some branches of the tree.

Therefore, this thesis describes an automated ex-vivo airway segmentation algorithm for micro-CT images of mouse lung which can thereby address the problems of previous methods and manual segmentation of the mouse lung airway tree. The major contribution of this algorithm, as described in the next section, is its application on an excised mice lung micro-CT scans to detect greater number of airways as compared to in-vivo airway tree segmentation algorithms.

## 2.6 Significance and Innovation of the work

Despite successes in the formulation of an in-vivo mouse airway segmentation algorithm (Figure 3(d)), doing the same for an ex-vivo mouse lung (Figure 3(c)), is ridden with challenges because of the comparatively thinner walls and also the minimal contrast between the airways and the vasculature. This is due to the fact that a fixed lung as a similar contrast for the airways and vasculature as both of them are filled with air (unlike in the case of an in-vivo scan where the airways are filled with air and vasculature with blood). Also, the segmentation of an ex-vivo scan (Figure 3(a)), allows the detection of the terminal branches of airways which escape the in-vivo scan (Figure 3(b)) due to the poor resolution and quality of the scans.

Apart from these primary advantages, the resultant segmented airway can also be used to find an approximate 3D region around the mediastinum, for smoothing the lung segmentation. Also, airway tree anatomical generation is used to establish a consistent criterion for airway inclusion or exclusion during lung segmentation.

An application of the ex-vivo airway segmentation technique described in the chapters to follow can help clinicians by qualitatively improving the precision of the diagnosis, facilitating better investigation of its causes and nature, and ensuring a more informed and effective administration of therapeutic drugs. By thus addressing the relatively lesser explored and partially uncertain aspects of the diagnosis of this dangerous disease, the technique explored in this thesis can cater to the needs of many throughout the face of the world.

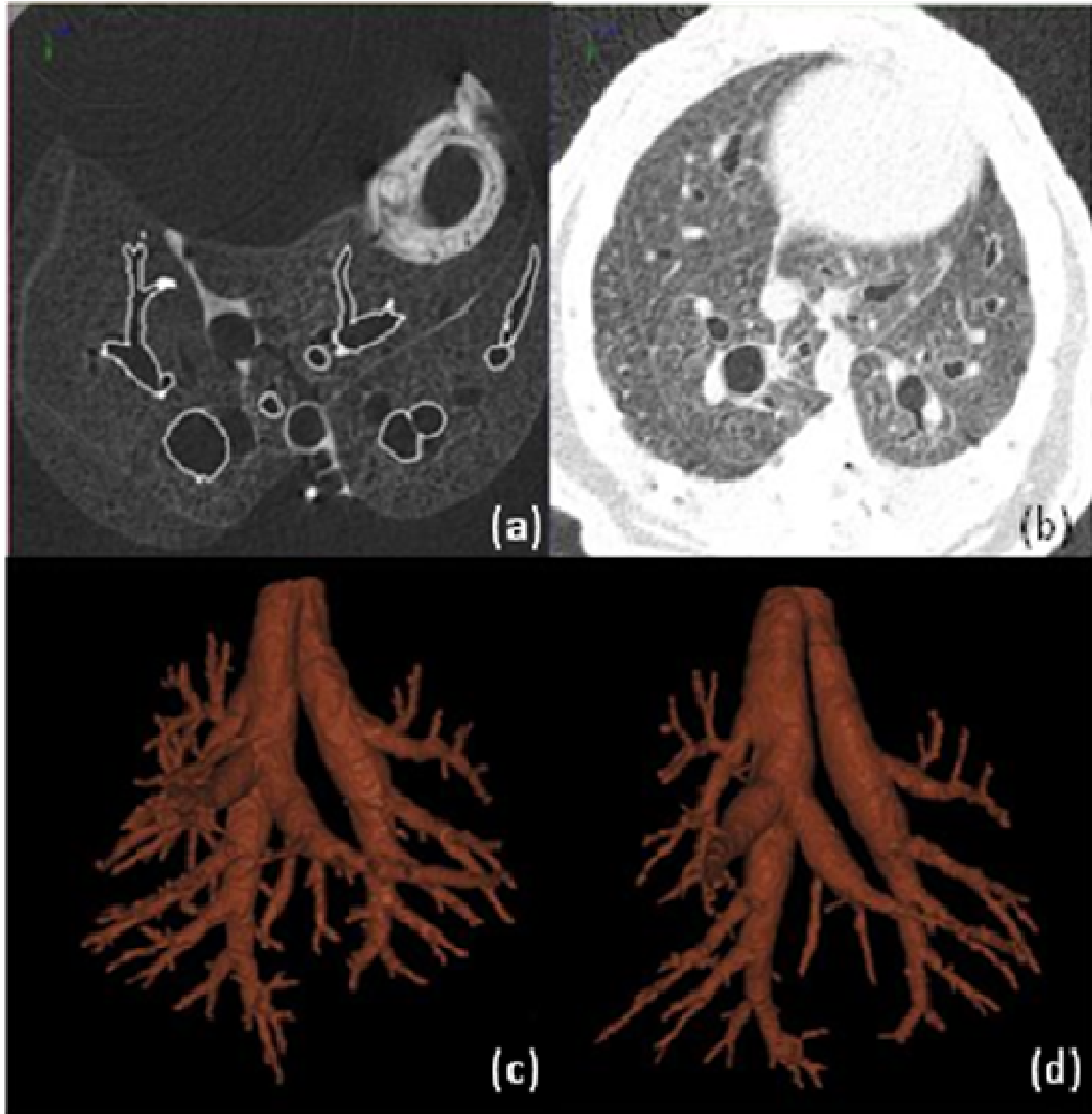


Figure 3. Comparison between the ex-vivo and in-vivo scans (a) Ex-vivo micro-CT scan, (b) In-vivo micro-CT scan, with airway segmentation (c) Volume rendered ex-vivo segmented tree (d) Volume rendered ex-vivo segmented tree

## CHAPTER 3 METHODOLOGY

### 3.1 Overview

The biggest challenge in segmenting an ex-vivo mice airway tree is that (as described in section 2.6) it has similar intensity for the airway and vasculature region. This justifies the need to develop an algorithm which can distinguish them based on local image appearance features. The major departure that this methodology makes from previous models is that its classification of voxels is based on the local image feature appearances unlike in cases of classification by voxel intensities [12].

However, the ground truth for training the classifier to segment the airways the excised mouse lung volume scans was obtained by the slice by slice manual analysis. Initially, rough airway segmentation is obtained by an automatic segmentation tool of a commercial software package. Then, the manual observer corrected any imperfections in all the slices by a manual airway contour editing tool. This usually took a week's time for analysis of a single scan. In order to automate the whole process of manual segmentation, this research study proposes a method that classifies the voxels into airway and non-airway kinds to arrive at the segmentation of an ex-vivo mouse airway tree. The overall method in this work is as shown in figure 4.

For the purpose of this research, image acquisition of a fixed excised lung specimen is performed on a Siemens Imtek Micro-CAT II, shown in figure 2, using the following parameters: 50kV, 200microAmp, 2500ms exposure time, detector binning of 2,720 projections over 270 degrees and 100 dark and 100 light images prior to each scan for calibration purposes. The reconstructed images were 1536 x 1536 x 1024 pixels in size when reconstructed using a 28 micron isotropic voxels. The field of view of the images is 43 x 43 x 28 mm. Due to the very long exposure time it is necessary to avoid

any movement caused by the ventilating airflow inside the scanner. Therefore the lungs were placed inside a sealed tube suspended on a thin suture string within the tube to avoid any contact to the walls of the tube.

An important step in preprocessing stage is to select the voxels inside the lung region of the image for classification. As we know that airways are always inside the lung region, analysis of the lung region voxels was sufficient for this method. The lung segmentation of the images was easy to obtain by semi-automatic and automatic methods. This step greatly helped in reducing computation time and memory. The processing method can be broadly divided into two phases – the training phase and the testing phase. In the training phase, the input is a micro-CT image whose features are extracted as described in section 3.2. These features are sent to the KNN-classifier (section 3.5) which gives the indices of the voxel that is close (by distance) to the image voxel to be classified. In the process of classifying voxels into airway and non-airway, a probability image is generated. A region growing segmentation algorithm is performed on the probability image obtained from the classifier in the previous step. The final segmentation results are adjusted with a manual threshold level for optimization.

The feature calculation method is described in section 3.2. The selection of the sample of voxels is as shown in section 3.3. The method to select best suited features for training the classifier is described in section 3.4. A detailed description of the KNN classifier is given in section 3.5.

### 3.2 Feature Calculation

In order to classify the voxels depending on their texture, shape, and locations, different features have been calculated. The image to be segmented is representative of the image intensities for the region growing approach. A set of 147 features that includes 21 different local image descriptors calculated at 7 different scales are used (Table 1).

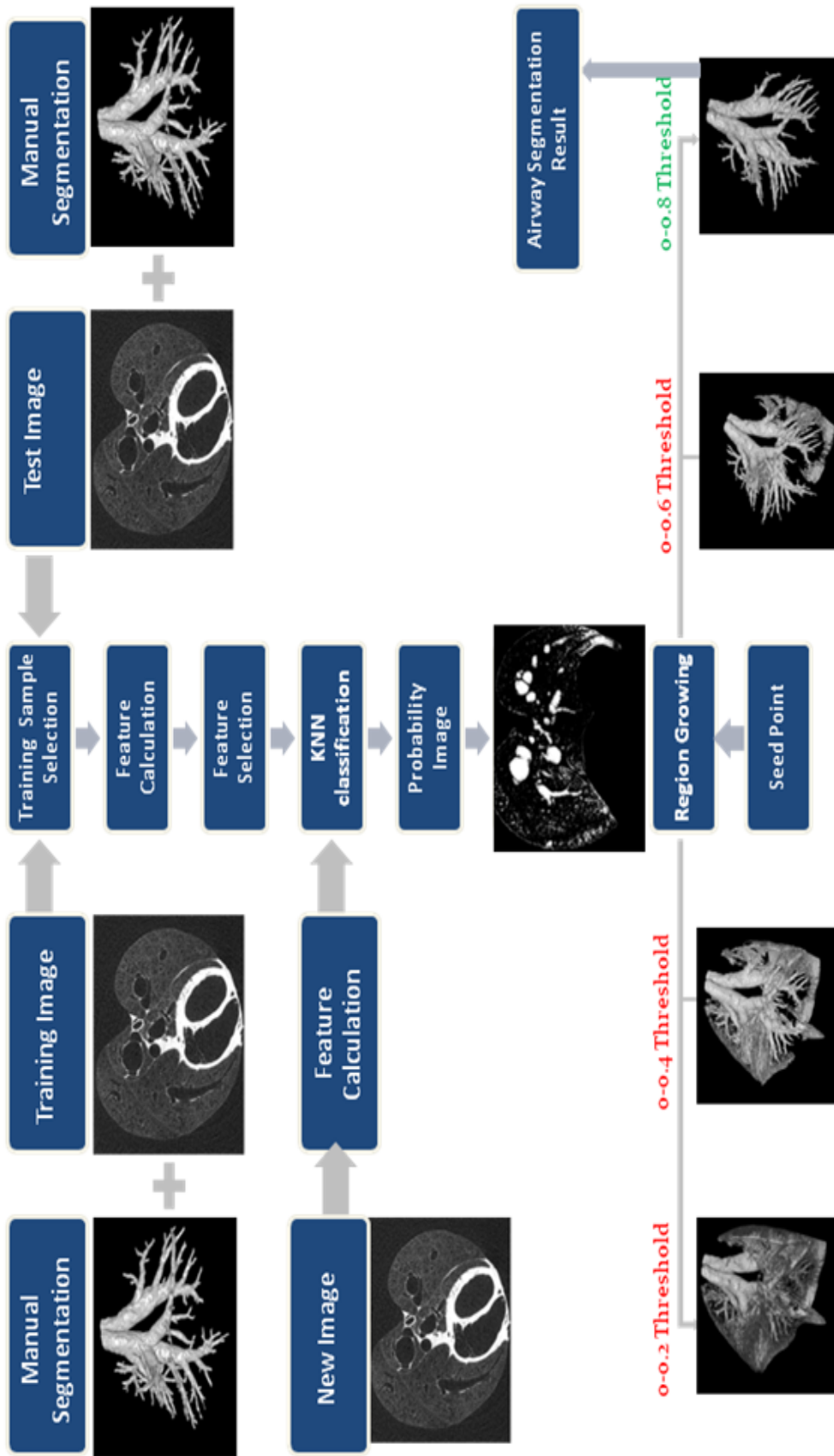


Figure 4. Overview of the method

The scale determines the amount of smoothing (standard deviation) for the Gaussian kernel. The set includes the smoothing and derivative image descriptors (Gaussian, first order derivative, second order derivative), rotationally invariant descriptors (gradient magnitude, Laplacian and Gaussian curvature) and shape descriptors (eigen values of Hessian, eigen values and eigen magnitude).

The following is the detailed description of all the above features used for classification:

1. *Convolution with Gaussian* ( $L=I * G$ ): In order to involve a smoothing operator, feature images are calculated by convolving it with the Gaussian kernel at 7 different scales. The convolution of the Gaussian smoothing operator  $G$  'blurs' the images and removes detail and noise. The Gaussian filter uses the following normal distribution equation for calculating the transformation to apply to each voxel in the image. The operator represents the shape of a Gaussian ('bell-shaped') hump; figure 5.

$$G(x, y, z) = \frac{1}{2\prod\sigma^2} \exp\left(-\frac{|x|^2 + |y|^2 + |z|^2}{2\sigma^2}\right), \quad -\infty < x, y, z < \infty$$

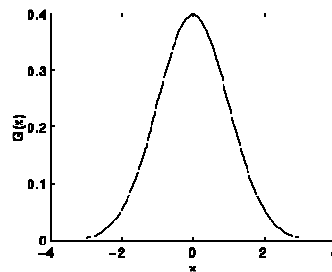


Figure 5. Gaussian distribution with mean 0 and Standard Deviation



Local Image Descriptor description	Name of the feature	Equation
Smoothing	Convolution with Gaussian	$(L = I * G)$
Derivative	First order derivative	$(L_x, L_y, L_z)$
Derivative	Second order derivative	$(L_{xx}, L_{yy}, L_{zz}, L_{xy}, L_{xz}, L_{yz})$
Rotationally invariant descriptor	Gradient magnitude	$(\sqrt{L_x^2 + L_y^2 + L_z^2})$
Rotationally invariant descriptor	Laplacian	$(\lambda_1 + \lambda_2 + \lambda_3)$
Rotationally invariant descriptor	Gaussian curvature	$(\lambda_1 * \lambda_2 * \lambda_3)$
Shape descriptor	Eigen values of Hessian	$(\lambda_1, \lambda_2, \lambda_3)$
Shape descriptor	Eigen magnitude	$(\sqrt{\lambda_1^2 + \lambda_2^2 + \lambda_3^2})$
Shape descriptor	Ratios of eigen values	$(\frac{ \lambda_3 }{\sqrt{ \lambda_1 * \lambda_2 }}, (\frac{ \lambda_2 }{ \lambda_1 }),$ $(\frac{ \lambda_3 }{ \lambda_1 }), (\frac{ \lambda_1  -  \lambda_2 }{ \lambda_1  +  \lambda_2 })$

Table 1. Table showing the set of 21 features calculated at 7 scales with corresponding equations assuming  $|\lambda_1| \geq |\lambda_2| \geq |\lambda_3|$

2. *First Order Derivative* ( $L_x, L_y, L_z$ ): The first order derivative of an image helps in marking the edges in the image. This is because of the fact that at the location of an edge there is a discontinuity in the intensity function or a very steep gradient in the image. Thus by taking the derivative of intensity across the image and find points where the derivative is a maximum the edges in the image can be detected.

$$\nabla I = \left[ \frac{\partial I}{\partial x}, \frac{\partial I}{\partial y}, \frac{\partial I}{\partial z} \right]$$

Thus the first order derivative of an image can be found by the following procedure:

- a) Convolving the image with a Gaussian mask to smooth it, then
  - b) Calculate derivatives of the smoothed image.
3. *Gradient Magnitude* ( $\sqrt{L_x^2 + L_y^2 + L_z^2}$ ): This feature is mainly used to determine the object contours and separation of homogenous regions. In other words, this feature is mainly used for edge detection in the image. It is given by:

$$GM = \sqrt{\left(\frac{\partial I}{\partial x}\right)^2 + \left(\frac{\partial I}{\partial y}\right)^2 + \left(\frac{\partial I}{\partial z}\right)^2}$$

4. *Second order derivative* ( $L_{xx}, L_{yy}, L_{zz}, L_{xy}, L_{xz}, L_{yz}$ ): Another feature image that marks an edge by a significant spatial change is the second order derivative of an image. Second order derivative information can also be used to extract local shape and orientation from a gray-scale image [16]. When a second

derivative of Gaussian is convolved with the image, we get a second order derivative image.

5. *Laplacian*( $\lambda_1 + \lambda_2 + \lambda_3$ ): As we know, the Laplacian operator is a measure of the second spatial derivative of an image. This feature particularly highlights the regions of rapid intensity change and is therefore used to detect edges. It is very important in the scale-space analysis of the image. To get the horizontal and vertical and depth edges we look at second derivatives in the x, y and z directions. Thus, the Laplacian of an image is given by

$$\nabla^2 I = \frac{\partial^2 I}{\partial x^2} + \frac{\partial^2 I}{\partial y^2} + \frac{\partial^2 I}{\partial z^2}$$

6. *Eigen values of Hessian*( $\lambda_1, \lambda_2, \lambda_3$ ): According to Frangi [18] et al., the vesselness measure is obtained on the basis of all the eigen values of the Hessian. The Hessian Matrix is a square matrix of second order partial derivatives of a function. This eigen values of Hessian analysis is mainly used to extract the principal directions in which the second order structure of the image can be decomposed. An ellipsoid as shown in figure 6 is an intuitive tool for the design of geometric similarity measures and thus can be used to describe the second order structure of the image.

The elements of the Hessian matrix approximate the second order derivatives, and therefore encode the shape information – both qualitative and quantitative description of how the normal to iso-surface changes. The computation of the second derivatives of an image yields three terms.

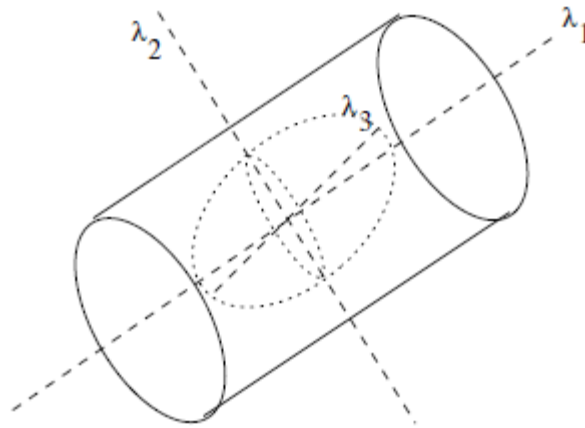


Figure 6. Second order ellipsoid describing the local principal directions of curvature [18]

While the Laplacian ignores one of them and considers every possible orientation at once, the Hessian takes all three terms into account and is orientation-dependent. The three Eigen values of the hessian matrix have the following property:

- a) Largest Hessian ( $\lambda_1$ ): The *Largest Hessian* operation determines the orientation along which the second derivative is maximal. It returns this maximum as a signed number
- b) Smallest Hessian ( $\lambda_3$ ): the orientation for which the second derivative is minimal can also be determined. The *Smallest Hessian* operation returns the minimum of the second derivative as a signed number.

The feature images that take into account the Eigen values play a crucial role in discriminating shape and orientation of structures. The following are the properties of the Eigen values as described by Frangi et al [18].

- Bright tubular structures will have low  $\lambda_1$  and large negative values of  $\lambda_2$  and  $\lambda_3$ . Conversely dark tubular structures will have a low value of  $\lambda_1$  and large positive values of  $\lambda_2$  and  $\lambda_3$ .
- Bright plate like structures has low values of  $\lambda_1$  and  $\lambda_2$  and large negative values of  $\lambda_3$ .
- Dark plate like structures has low values of  $\lambda_1$  and  $\lambda_2$  and large positive values of  $\lambda_3$ .
- Bright spherical (blob) like structures have all three eigen values as large negative numbers.
- Dark spherical (blob) like structures have all three Eigen values as large positive numbers [17].

Therefore, these values are very helpful in discriminating the Bright or dark tubular, blob or plate-like structures in the image.

$\lambda_1$	$\lambda_2$	$\lambda_3$	Orientation Pattern
N	N	N	Noisy, no preferred direction
L	L	H-	Plate-like structure (bright)
L	L	H+	Plate-like structure (dark)
L	H-	H-	Tubular structure (bright)
L	H+	H+	Tubular structure (dark)
H-	H-	H-	Blob-like structure (bright)
H+	H+	H+	Blob-like structure (dark)

Table 2. The Eigen values representing the possible patterns in the 3D image

Note: (H= High, L= Low, N = Noisy, usually small) +/- indicate the sign of the Eigen value. Ordered as  $|\lambda_1| \leq |\lambda_2| \leq |\lambda_3|$ . This table is from [18].

7. *Gaussian Curvature* ( $\lambda_1 * \lambda_2 * \lambda_3$ ) : Shape remains a major descriptive feature of objects in the morphometry of an image. The Gaussian curvature operator is a shape descriptor in which a positive Gaussian curvature value means the surface is locally either a peak or a valley. A negative value means the surface locally has a saddle points. And a zero value means the surface is flat in at least one direction (i.e., both a plane and a cylinder have zero Gaussian curvature) [18]. It is represented as the product of the Eigen values of the Hessian Matrix i.e.

$$\text{Gaussian Curvature} = \lambda_1 \times \lambda_2 \times \lambda_3$$

8. *Eigen Magnitude* ( $\sqrt{\lambda_1^2 + \lambda_2^2 + \lambda_3^2}$ ): In the micro-CAT images of the mouse lung, the airways are represented as bright tubular structure with a darker background. According to [17], for an ideal tubular structure in a 3D image should have

- a) The magnitude of the smallest Eigen value  $|\lambda_3| \approx 0$
- b) The difference between the magnitudes of the smallest Eigen value  $|\lambda_3|$  and the intermediate Eigen value  $|\lambda_2|$  should be high i.e.  $|\lambda_2| \ll |\lambda_3|$
- c) The intermediate Eigen value ( $\lambda_2$ ) and the largest Eigen ( $\lambda_1$ ) value should nearly be the same i.e.  $\lambda_3 \approx \lambda_2$

Thus, the Eigen magnitude image descriptor helps in determining the tubular structures.

9. *Ratios of Eigen Values*: The following ratios of the Eigen values help in distinguishing the shapes of the different structures [18]:

- a) The following ratio can be interpreted to consider any deviation from a

blob-like structure but cannot distinguish between a line and a plate like pattern. Thus, this ratio is maximum for a blob-like structure and zero whenever  $\lambda_1 \approx 0$  or when  $\lambda_3$  and  $\lambda_1$  tend to vanish (as the ratio  $(|\lambda_3|/|\lambda_1|)$  help in defining the bounds because even when the second Eigen value is small its magnitude is always larger than the first)

$$\left( \frac{|\lambda_3|}{\sqrt{|\lambda_1 * \lambda_2|}} \right)$$

- b) The following set of ratios help in distinguishing between the plate-like and line-like structures. For e.g. the ratio is zero for a line-like structure. The above ratios are grey-level invariant i.e. they do not depend on the intensity rescaling. Hence, these features determine only the geometric information in the image.

$$\left( \frac{|\lambda_2|}{|\lambda_1|} \right)$$

- c) The following ratio is a normalization measure of planeness of the structure in the image. Thus, this ratio is 1 for one significant Eigen value  $\lambda_1$  and two vanishing Eigen values  $\lambda_2$  and  $\lambda_3$  and 0 if the two most significant Eigen values are equal.

$$\left( \frac{|\lambda_1| - |\lambda_2|}{|\lambda_1| + |\lambda_2|} \right)$$

In all there are 21 different features for an image which are calculated over equal intervals of standard deviation values ( $\sigma$ ) ranging from 0.01 to 3. The 147 features calculated for both training and testing images are the inputs for the KNN classifier (as data and query points). The detailed description of the selection of the best features from the given set of 147 features is given in the section 3.4.

### 3.3 Training Sample Selection

As explained in the previous section, the voxels in an image are classified into airway and non-airway based on the features calculated as per section 3.1 by the KNN classifier. However, the research does not necessitate the classification of all the image voxels as the few that are chosen (according to the principle explained in this section) are representative of the whole sample of airway and non-airway voxels. The process of selecting a sample of voxels for the KNN classifier training instead of working on the whole body of voxels is crucial given the constraints of time and memory.

However, it is equally important to adopt a proper procedure for selecting the sample. This is because a random selection would introduce a bias towards the larger airways. This happens since voxels from the larger airway automatically get selected because they are present in larger volumes in the scan. In order to avoid such skewed results, a distance transform is used during the sample selection process.

The Euclidean distance of all the airway voxels from a seed point in the Trachea is calculated. The voxels are placed into a fixed number of bins based on their sorted distances. This ensures that all the voxels that are closer to the Trachea are put into one set of bins and those which are farther would be put into another set of bins. A fixed percentage of airway voxels are selected as samples from each bin by random sampling.

In the context of this research, the non-airway region has been taken to imply the region surrounding the airways in the training phase. The region around the airways is



obtained by dilating the airway voxels over a radius of 7 voxels and then subtracting the original airway voxels from them. The sample of the non-airway voxels from this region is selected by random sampling.

The airway voxels and the non-airway voxels in the central slice for the same scan are shown in figure 7.

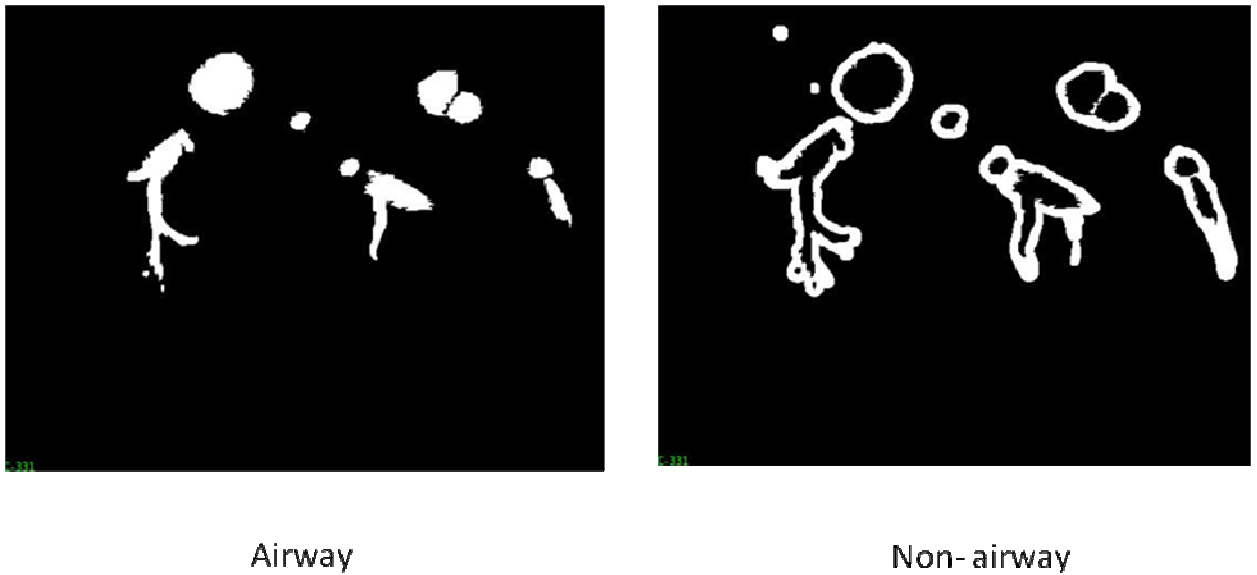


Figure 7. Mid-slice sample selection of Airway and Non-airway voxel

### 3.4 Feature Selection

Feature selection is the most critical stage in the entire process of segmenting the airways from the lung as this stage helps to determine the best suited set of features in a way that make the precise and accurate classification of airways and non-airways possible. Using all the features calculated as per section 3.1 might not ensure the accuracy of KNN classification. From the set of 147 potential features, the number of features to be chosen for an accurate KNN-classification is based on the improvement curve of the criterion value. The process of determining the criterion value has been

explained later in the chapter. The selection of the best suited select features is stopped when a saturation point is reached with respect to the criterion value.

The procedure to select best features is based on the Sequential Forward Selection (SFS) floating search algorithm [19] as in figure 8. Initially the set of best features is defined empty. As the selection process continues, the features with the best combined performance are added one after the other. The combined performance of the features added to the set is evaluated based on a criterion value. The optimization criterion for adding the feature to the set of select features is reached by maximizing the area under the Receiver Operating Characteristic (ROC) curve.

The area under the ROC curve helps in determining if the positives are ranked higher than the negatives. It has an interesting property to give the costs for different kinds of misclassification. The points on the ROC curve determine the optimum threshold for the region growing algorithm in the final step of segmentation.

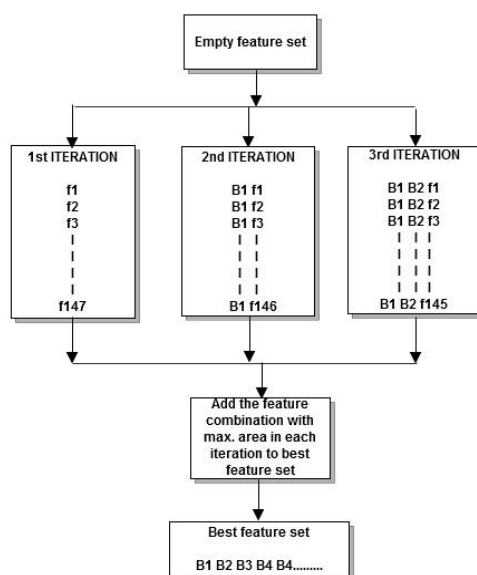


Figure 8. Sequential forward floating search process (f1, f2 ...f147 – feature values and B1, B2, B3 – best features selected in the previous iteration)

In case of identifying the set of features which accurately classify the airway and non-airway voxels of the image, each feature image of the training and testing data set is added individually to the existing set of features. For each feature that is added, the voxels are fed into the KNN-classifier and a probability value is generated for each voxel in the testing image. The probability image is thresholded into four different ranges of intensity, that is, 0-0.2, 0-0.4, 0-0.6 and 0-0.8. All the intermediate thresholded images are compared with the ground-truth of the testing image to determine the true positives and true negatives.

The sensitivity of the classification is determined by taking the ratio of the true positives (the number of correctly classified airway voxels) to the sum of true positives and false negatives comparing to the ground-truth image (the number of correctly classified airway and incorrectly classified non-airway voxels). In other words it is given by the formula:

$$Sensitivity = \frac{\text{number of true positives}}{\text{number of true positives} + \text{number of false negatives}}$$

Similarly, the specificity of the classification is determined by taking the ratio of the true negatives (the number of correctly classified non-airway voxels) to the sum of false positives and true negatives in the ground-truth image (the number of incorrectly classified airway and correctly classified non-airway voxels). In other words it is given by the formula:

$$Specificity = \frac{\text{number of true negatives}}{\text{number of false positives} + \text{number of true negatives}}$$

The specificity and sensitivity values for thresholded images are calculated and plotted. The graph plotted for the sensitivity and 1- specificity value for the four ranges of values is the required ROC curve. The trapezoidal rule for calculating the area under the ROC curve is implemented wherein the areas of the individual trapezoids formed by the points in the graph are summed up to calculate the total area under the curve.

The optimization process to maximize the area under the ROC curve given by the classification of the best combination of features is carried out by including the feature to combination of features which increases the area the flow of the implementation of the best feature selection is shown in figure 9.

### 3.5 KNN-Classification

In the k-nearest neighbor searching problem, the KNN classifier is used for a non-parametric supervised pattern classification [20]. The KNN classifier can classify the set of given points in an n-dimensional space into particular groups based on the distances measured between the points in the training and testing data sets. This classifier does not require any prior knowledge about the distribution of the data points.

The points to be classified (testing data set) are fed to the KNN classifier such that for any given query point, the KNN searches its nearest neighbors from the k-d tree data structure formed by set of training points. The number of nearest neighbors (k value) to be obtained from the classifier is user defined and can be changed according to the obtained criterion value for the feature selection process as explained in section 3.2. KNN classifier returns the indices of the nearest neighbors in the training data set which are closest in distance to the given query point. The running time or the space of the KNN classifier grows exponentially with an n-dimensional space.

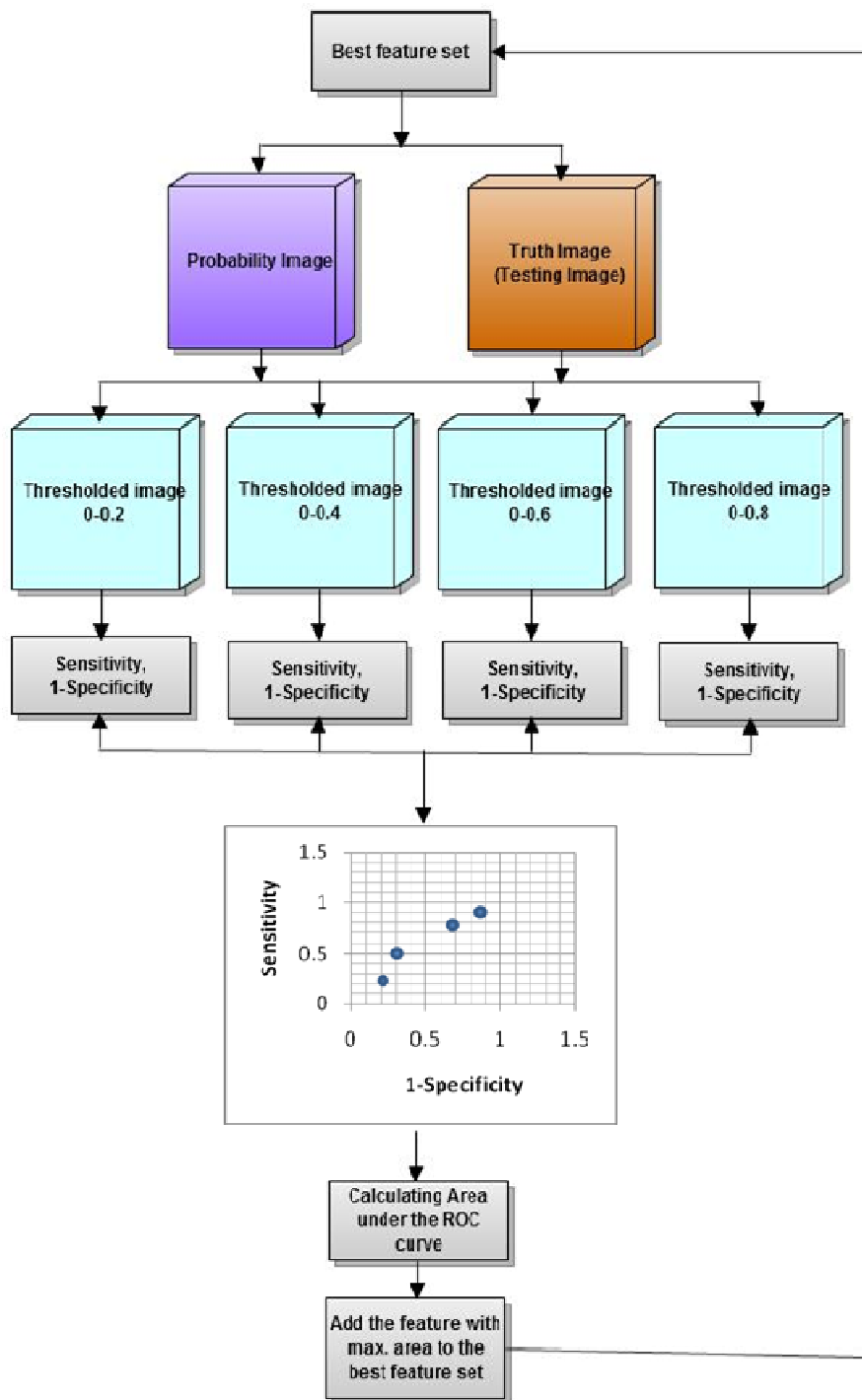


Figure 9. Flow chart of selecting the set of best features by the Feature Selection method

For example as shown in figure 10, there are a total of 23 sample points and a single query point scattered over in a 2 dimensional feature space. The Minkowski distances [13] or the simple Euclidean distance to each of the 23 sample points from the query point is calculated. In the above case,  $k$  is defined as 4. Among, the four nearest neighbors of the test sample, the most frequent class label color is red, and thus the test sample is assigned to the class A.

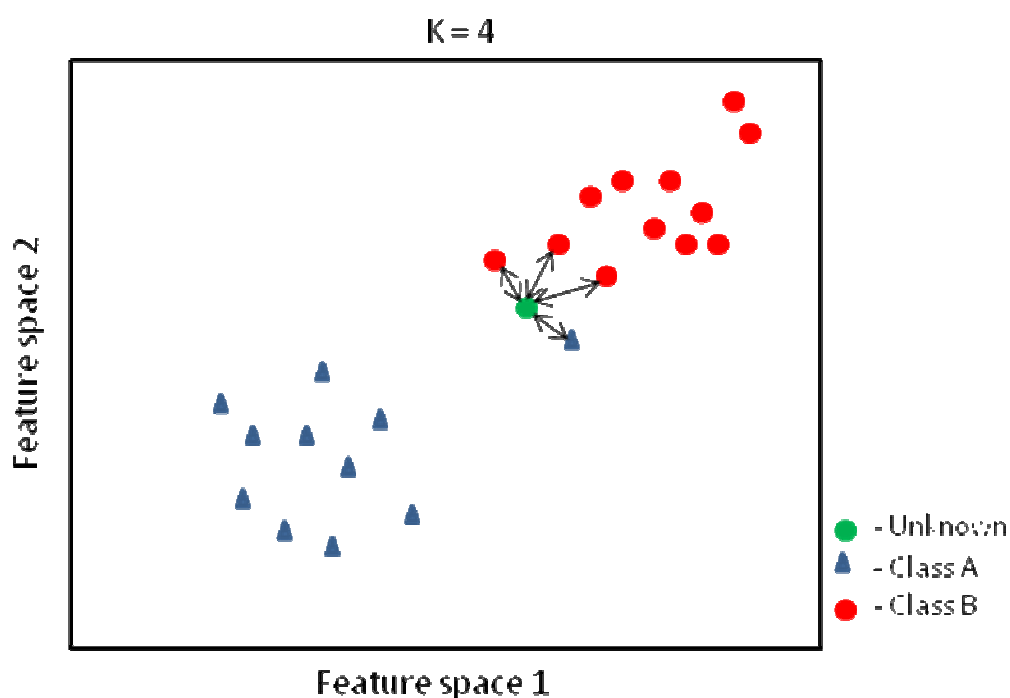


Figure 10. X-Y scatter plot of a 2 dimensional feature space with 23 samples for KNN-classification ( $k = 4$ ).

If a brute force process of computing the distances between the query point and each of the data points is applied, then this may be too slow for the current application. An Approximate nearest neighbor searching (ANN) library [13] that preprocesses the

data points into kd-tree data structure from which nearest neighbor distances are computed is used to overcome this problem (section 3.6).

The classification of the voxels in the image into two different classes – airway and non-airway is performed to obtain a probability image for the final airway segmentation. The classifier is trained on the feature values of voxels from the two different classes of voxels in the training image. Each point from testing image is classified into either of these classes depending on the number and type of nearest neighbors returned by the classifier. The gray-scale values for each voxel in the probability image returned by the classifier represent the chance of that voxel in the testing image to be an airway or a non-airway.

### 3.6 Implementation details

In the feature calculation step, the convolved image with the Gaussian kernel is calculated by applying a Gaussian filter is separately along each direction of the image. The filter in ITK “RecursiveGaussianImageFilter” applies the approximation of convolution with the Gaussian in a single dimension. Several of these filters are concatenated to obtain smoothing in all directions. The same filter in ITK is used to calculate the first and second order derivatives of the image [14]. The gradient magnitude of the image is computed by convolving the image with the Gaussian mask and then adding the sum of the squares and computing the square root of the sum. The ITK filter “GradientMagnitudeImageFilter” computes the magnitude of the image gradient at each pixel location using a simple finite differences approach. The second order derivatives from each direction are added together to obtain the Laplacian operator.

The KNN classifier library used in this research work is a built-in library in C++ named ANN is used to search the nearest neighbor voxels in spaces of various dimensions in an approximate or exact manner [13]. In the current implementation of the

classifier to classify the voxels of the testing image into airway and non-airway, the number of nearest neighbors to be returned by the classifier is set to 15. This means that for every voxel in the testing image, the indices of 15 voxels of the training image which are closest in distance are returned. The indices are cross-checked with the ground-truth of the testing image to determine if they represent the airway or non-airway voxels. The probability of every voxel is calculated by taking the ratio of the number of airway indices returned by the classifier to the total number of nearest neighbors for that voxel (15). The higher the probability value of the voxel nearing the value of 1, the greater is its chances of being an airway (ideally 1) while the lower the intensity value nearing the 0, the greater are its chances of being a non-airway (ideally 0). The diagrammatic flow of the image construction is shown in the figure 11.

One of the main advantages of this library is the ability to allow user to achieve significant improvements in the running time by tolerating a small amount of error (Epsilon) in the search. This means that the classifier returns a point that may not be the nearest neighbor, but is not significantly further away from the query point than the true nearest neighbor. In other words, when the classifier returns  $k$  distinct nearest neighbor points from the sample set, such that  $1 \leq i \leq k$ , the ratio between the distance to the  $i^{\text{th}}$  reported point and the true  $i^{\text{th}}$  nearest neighbor is at most  $1 + \epsilon$ . This is called the approximate nearest neighbor searching where the error bound limit  $\epsilon$  (Epsilon) or EPS is user defined.

Another method implemented, in order to reduce the time for classification of each query voxel by ANN was by using a parallel processing thread-safe library named Simple, Thread-safe Approximate Nearest Neighbor (STANN) instead of ANN [22]. This library is known to be faster in the construction of  $k$ -nearest neighbor graphs, better in cache efficiency and minimal space utilization. It is based on the ANN library and Morton ordering for graph construction to parallel process features during classification.



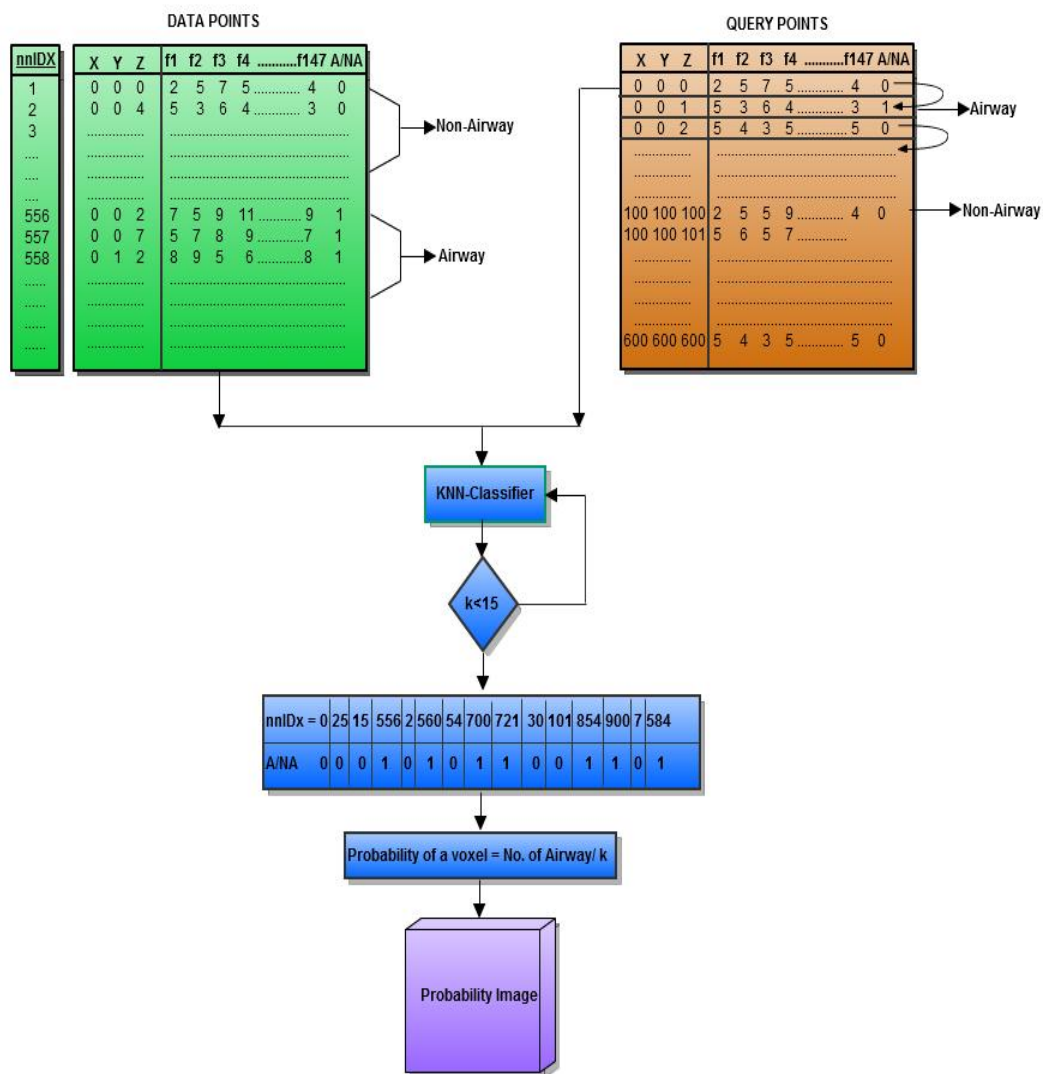


Figure 4. Flow chart of obtaining probability image from the KNN classifier

Further, the algorithm performs well for data sets which are too large to reside in the internal memory but is not suitable for higher dimensionality in the feature space (usually  $d > 5$ ). The comparison between the ANN and STANN performance on the micro-CT data is illustrated in section 4.3.

## CHAPTER 4

### RESULTS

#### 4.1 Feature Calculation Results

The feature images for a given CT lung volume are calculated at 7 different scales ranging from 0.01 to 3. The process by which the features are calculated is described in section 3.1. It is implemented such that all the points belonging to the airway class of the training data set are written into a text file by randomly selecting the voxels from the bins created by distance transform as mentioned in section 3.2. Similarly, the non-airway voxel features from the training data set are written to 7 different text files by random selection. All the test voxels inside the lung region are written in a similar way to text files to be read by the classifier. Some of the examples of the feature images at a mid-slice of the volume are as shown in figure 12.

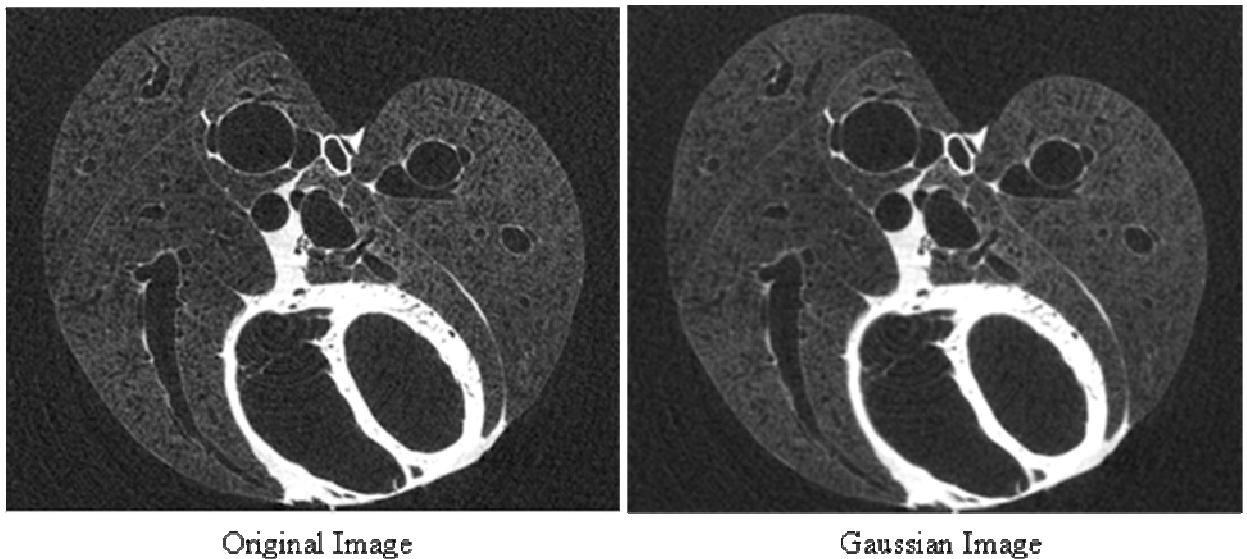
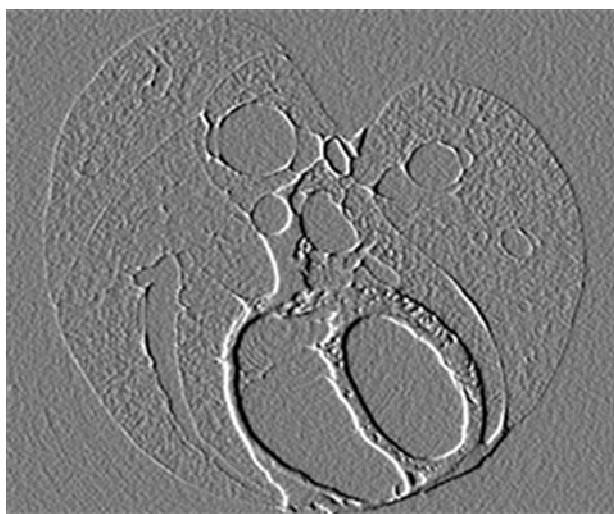
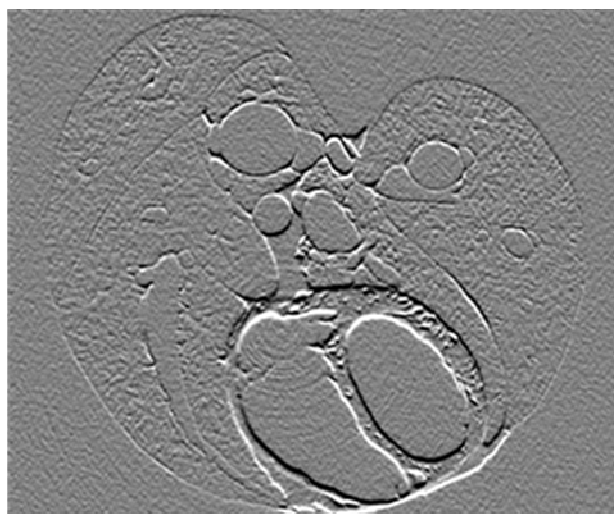
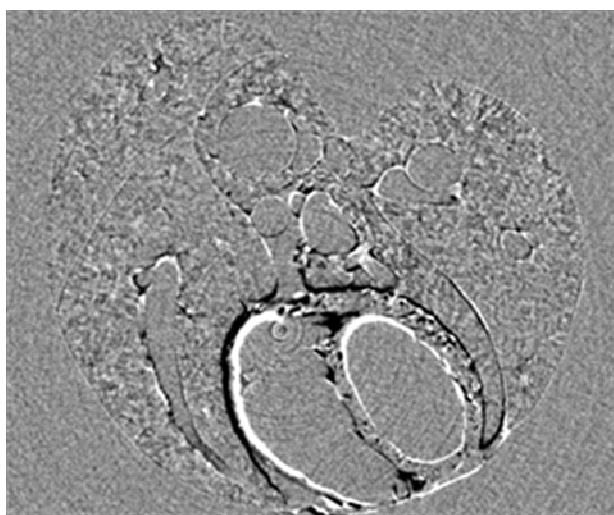


Figure 12 - continued

First Order Image -  $I_x$ First Order Image -  $I_y$ First Order Image -  $I_z$ 

Gradient Magnitude Image

Figure 12 - continued

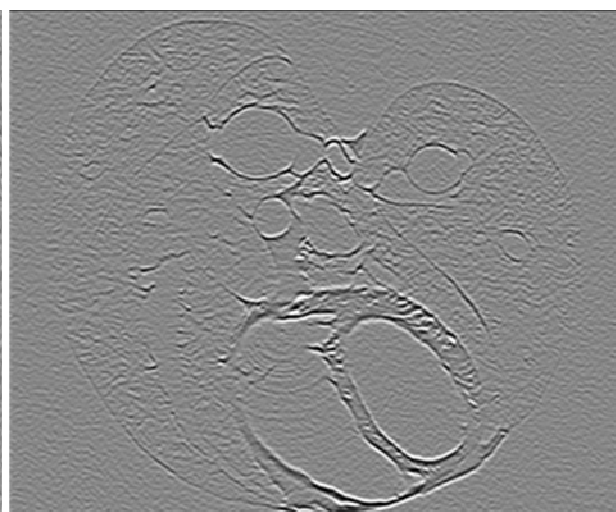
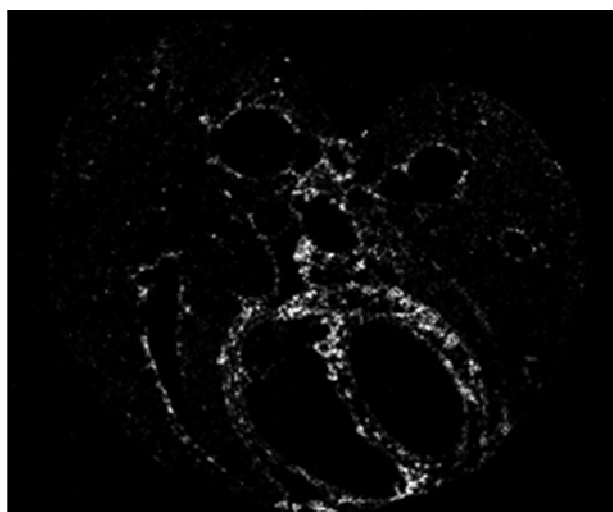
Second Order Image -  $I_{xx}$ Second Order Image -  $I_{xy}$ Second Order Image -  $I_{xz}$ Second Order Image -  $I_{yy}$ 

Figure 12 - continued

Second Order Image -  $I_{yz}$ Second Order Image -  $I_{zz}$ 

Laplacian Image

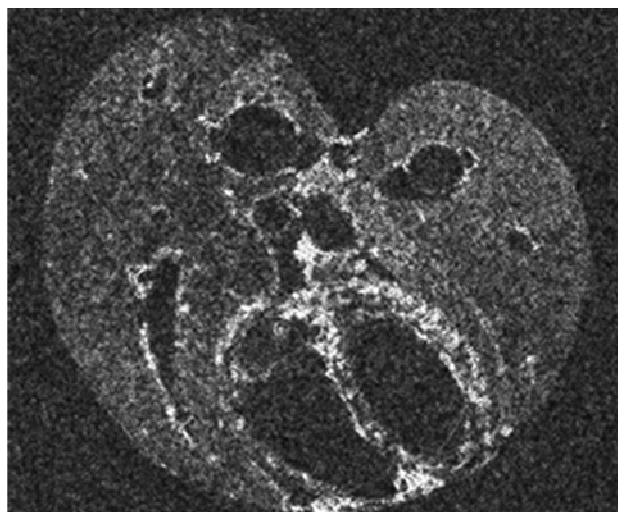


Gaussian Curvature Image

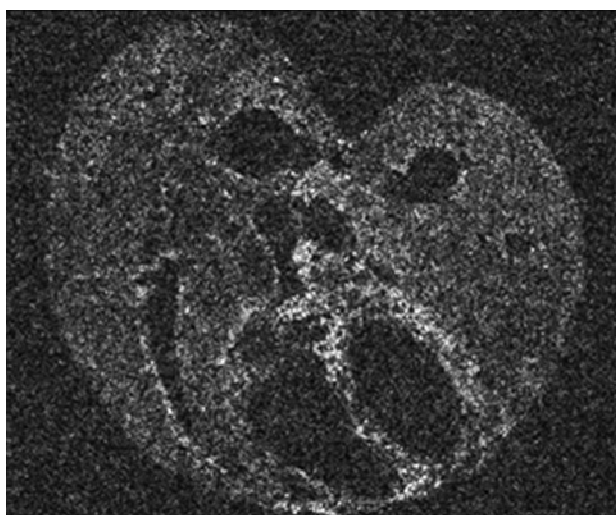
Figure 12 - continued



Hessian Image - 1



Hessian Image - 2



Hessian Image - 3

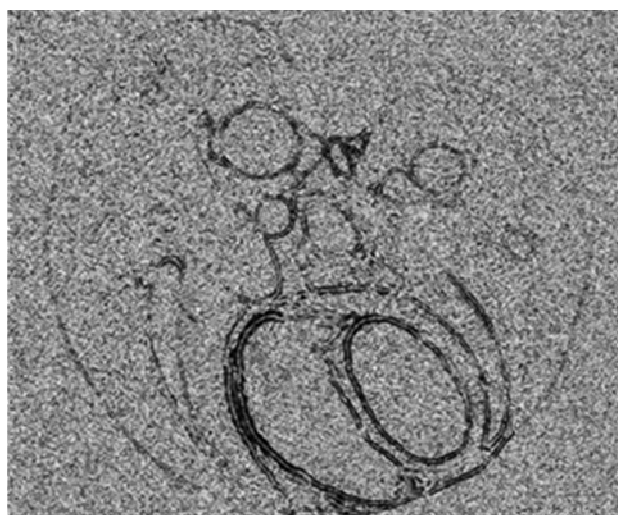
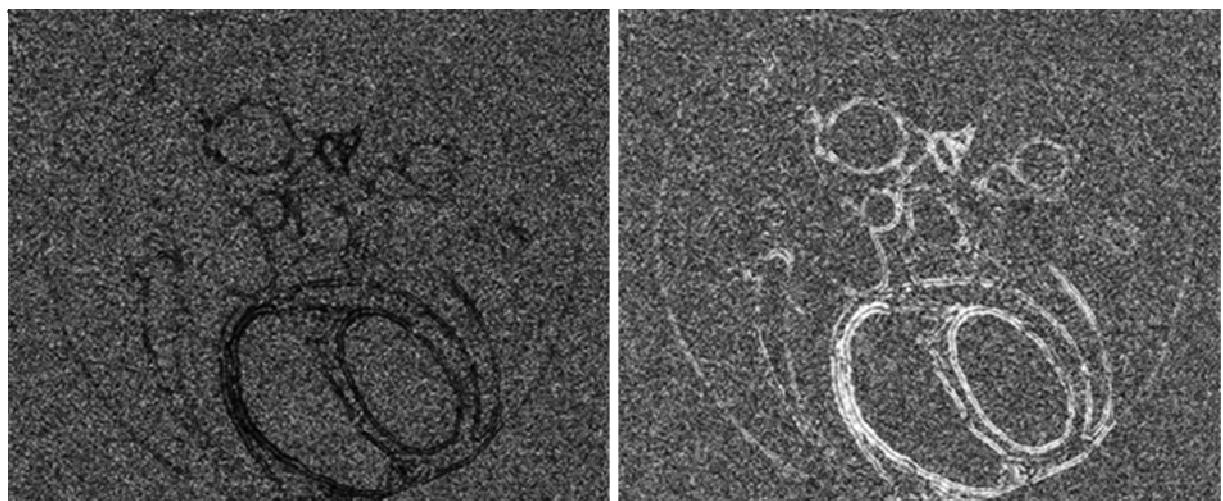
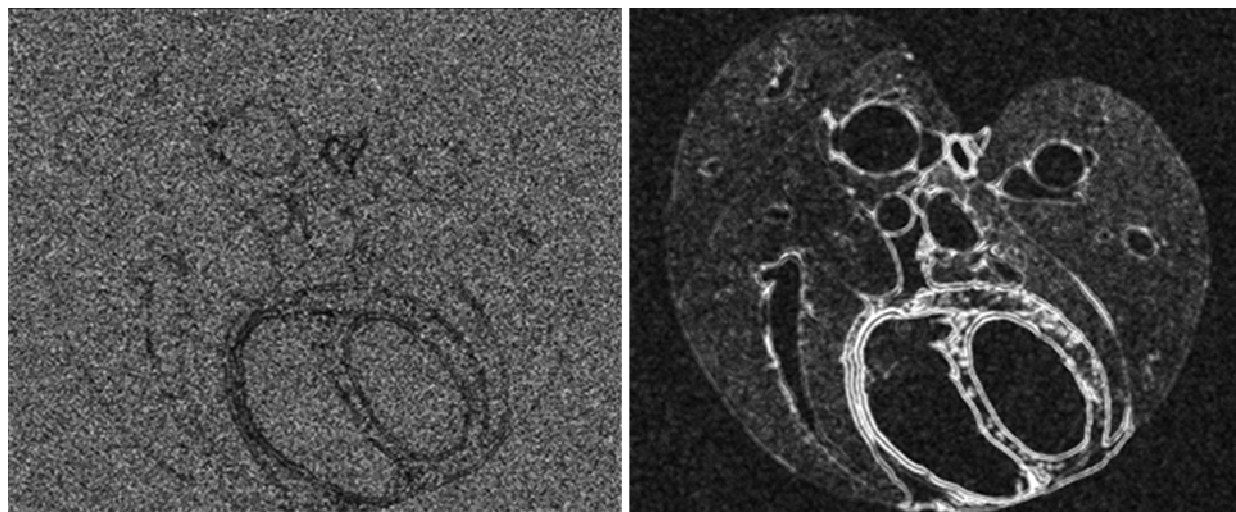
Ratio of Eigen Value Image ( $\lambda_2/|\lambda_1|$ )

Figure 12 - continued

Ratio of Eigen Value Image ( $|\lambda_3|/|\lambda_1|$ )Ratio of Eigen Value Image ( $|\lambda_1 - \lambda_2| / (|\lambda_1| - |\lambda_2|)$ )Ratio of Eigen Value Image ( $|\lambda_3|/\sqrt{|\lambda_1 \cdot \lambda_2|}$ )

Eigen Magnitude Image

Figure 12. The set of 21 local image descriptors (feature images) calculated at scale 1

These features are calculated with seven different standard deviations or scales.

#### 4.2 Results for the Selection of the Best Suited Features

After the features are calculated, the best suited features among them are selected based on their performance with respect to a criterion value. The feature selection procedure as illustrated in section 3.3 resulted in the following set of features as the best features. The selection procedure maximized the area under the ROC curve from 0.68 (for the first best feature selected) through 0.8 till the last feature is selected. The feature selection process is stopped when the area under the ROC curve reaches a saturation which is indicated by figure 13. There was no significant increase in the area under the ROC curve after the selection of 12 features.

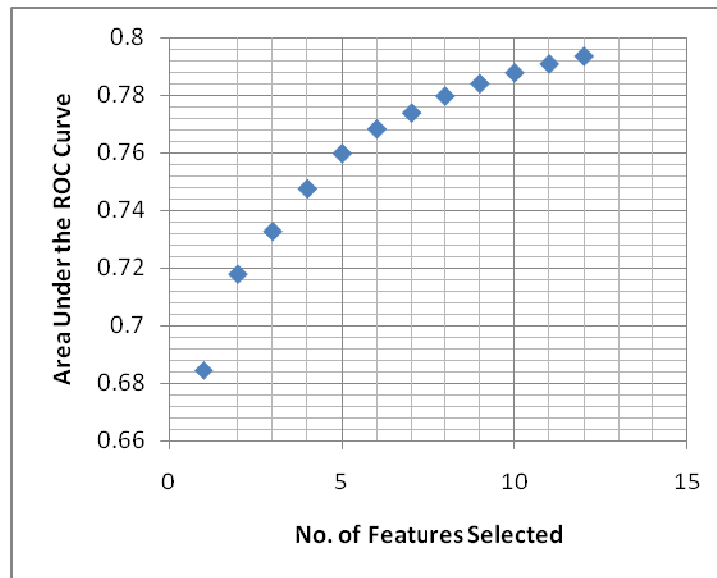


Figure 5. Graph showing the criterion value achieved with the increase in the number of features selected



We know that the classifier's performance is based on the type and the number of training points given to the classifier. In other words, the greater the number of training points in the data set, the better is the criterion value achieved (resulting in better classification) as shown in figure 14.

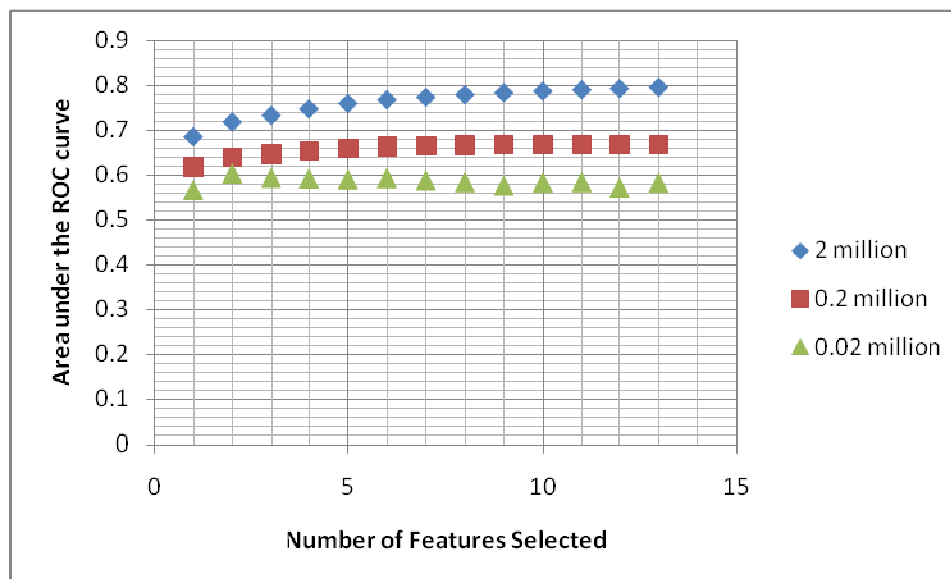


Figure 6. Graph showing the increase in the criterion value with changing number of training points

Table 3 gives the details of the various features selected by classifying a test data set of 2 million points based on the training set of 2 million points.

The feature numbers as used in the implementation part (based on their sigma set and type in the program) in this research study is listed in the appendix.

#### 4.3 KNN Classification Results

Figure 15 shows the output probability image obtained as a result of classification. It also shows the 4 different thresholded images after region growing in the range of 0-0.2, 0-0.4, 0-0.6 and 0-0.8 by setting the seed point in the Trachea

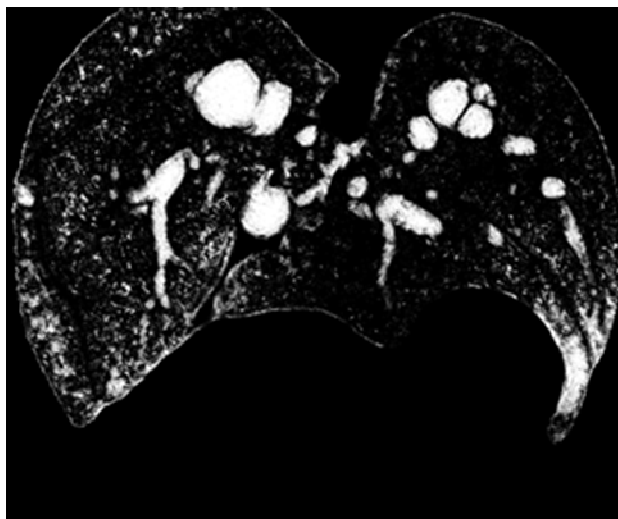
No.	Name of the Feature	Sigma	Area under the ROC curve
1	Gaussian Image	2	0.684248
2	Gradient Magnitude Image	0.5	0.717745
3	Eigen Magnitude Image	1	0.732584
4	Gradient Magnitude Image	1	0.747422
5	Eigen Magnitude Image	3	0.759701
6	Largest Eigen value of Hessian Image	2	0.768203
7	First Order Derivative in Y Image	3	0.773753
8	First Order Derivative in X Image	3	0.779643
9	Second Order Derivative in XX direction	3	0.783964
10	Second Order Derivative in XY direction	2	0.787715
11	First Order Derivative in Z direction	3	0.790821
12	Second Order Derivative in ZZ direction	2	0.793472
13	Eigen value of Hessian Image	3	0.796331

Table 3. Features selected during the feature selection method with their corresponding criterion value

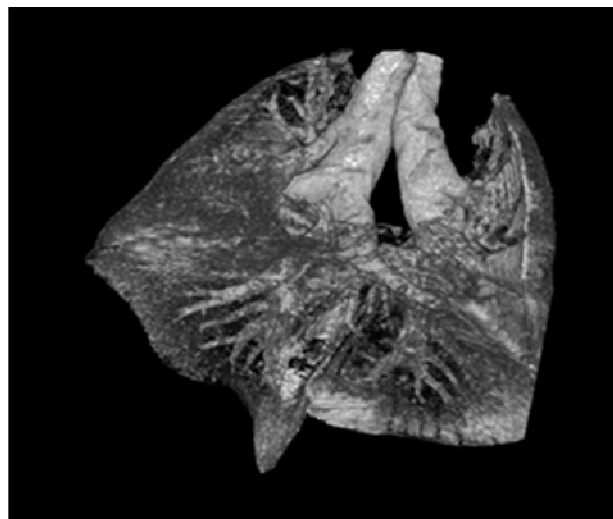
The sensitivity and the specificity values for the same data set are as plotted in figure 16 as per table 4.

Threshold Range	Sensitivity	1-Specificity
0-0.2	0.969969	0.038879
0-0.4	0.934031	0.020526
0-0.6	0.880215	0.007774
0-0.8	0.780267	0.001646

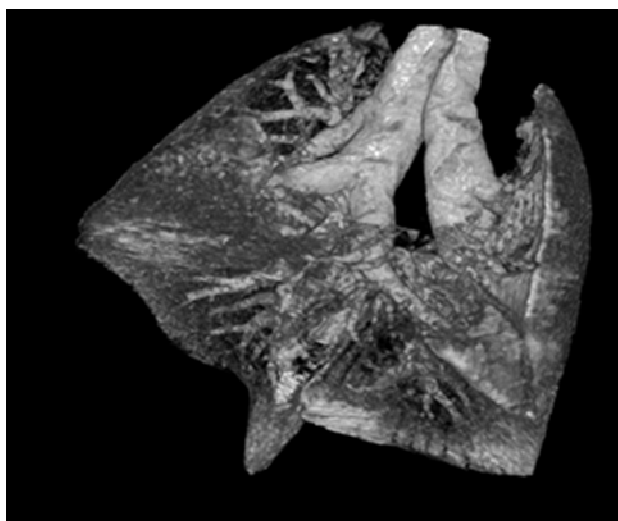
Table 4. Change in the specificity and sensitivity values across four threshold ranges



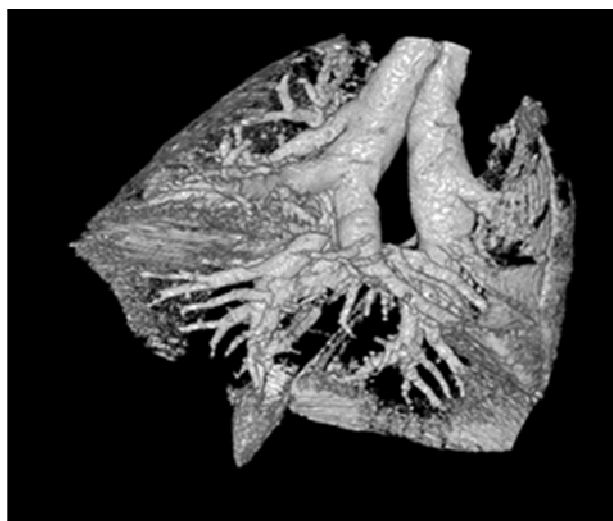
Mid slice of the probability image



Volume rendering of the probability image



Probability image thresholded to 0-0.2



Probability image thresholded to 0-0.4

Figure 15- continued

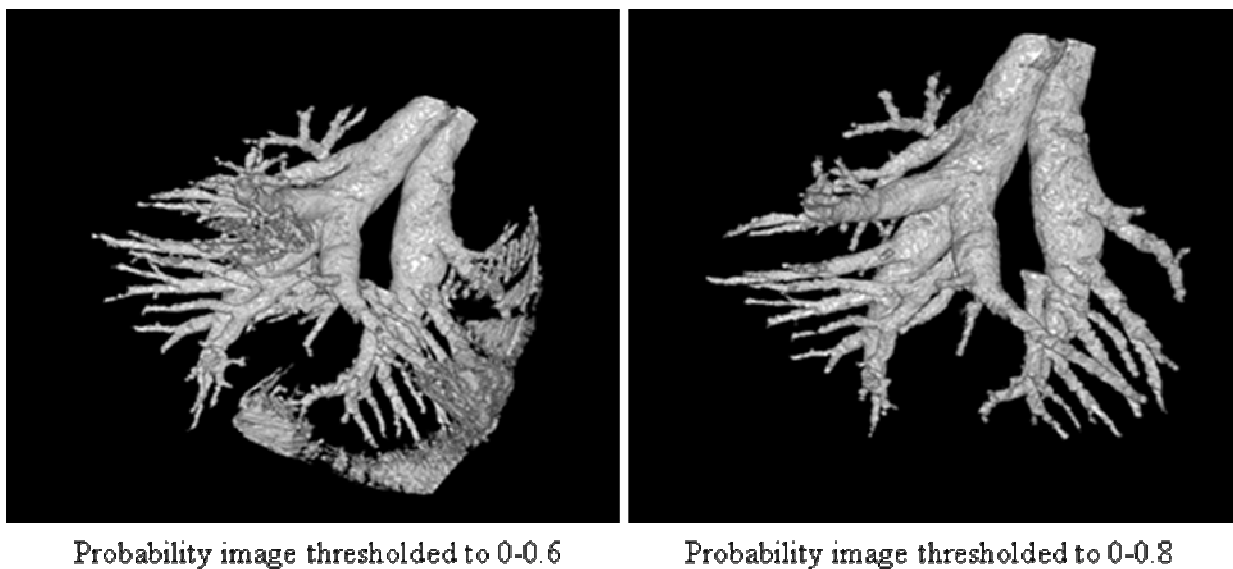


Figure 7. Probability images at 4 different thresholds of 0.2, 0.4, 0.6, and 0.8

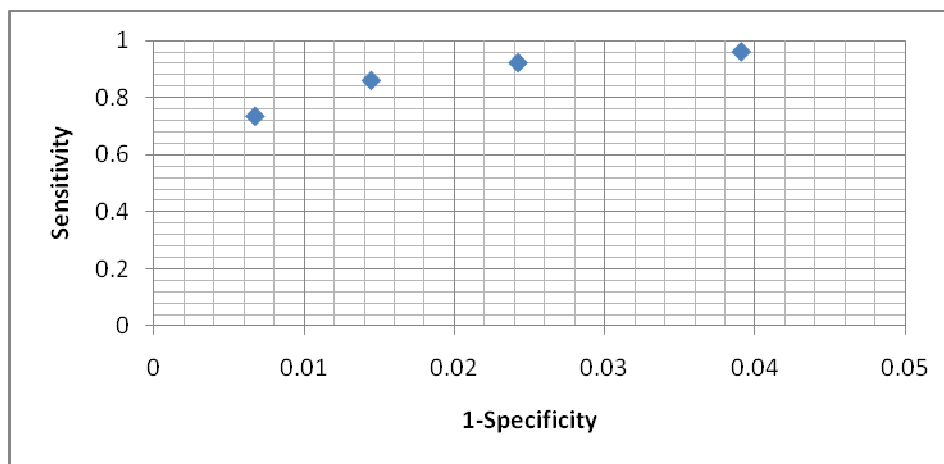


Figure 8. Graph showing the area under the ROC curve from four different threshold values

The above classification is performed and the airway segmentation is obtained on three different images based on the training with the same set of

features. Figure 17 shows the volume rendered airway tree results of the segmentation of three different CT scans. It also shows their sensitivity and specificity curves which have been obtained by comparing each voxel with its manual segmentation.

The time performance of the STANN library which is known to be a multi-thread safe library for the approximate nearest neighbor calculation is compared with the ANN library. The number of threads for the program is set to 1 to compare its time performance with the ANN. It is observed that the classification time for a smaller dimension in feature space is very good and it deteriorates as the dimension of the feature increases. Figure 18 shows the decrease in performance with the increase in the dimensionality of the feature space.

Figure 9. Volume rendered airway segmentation for three different scans

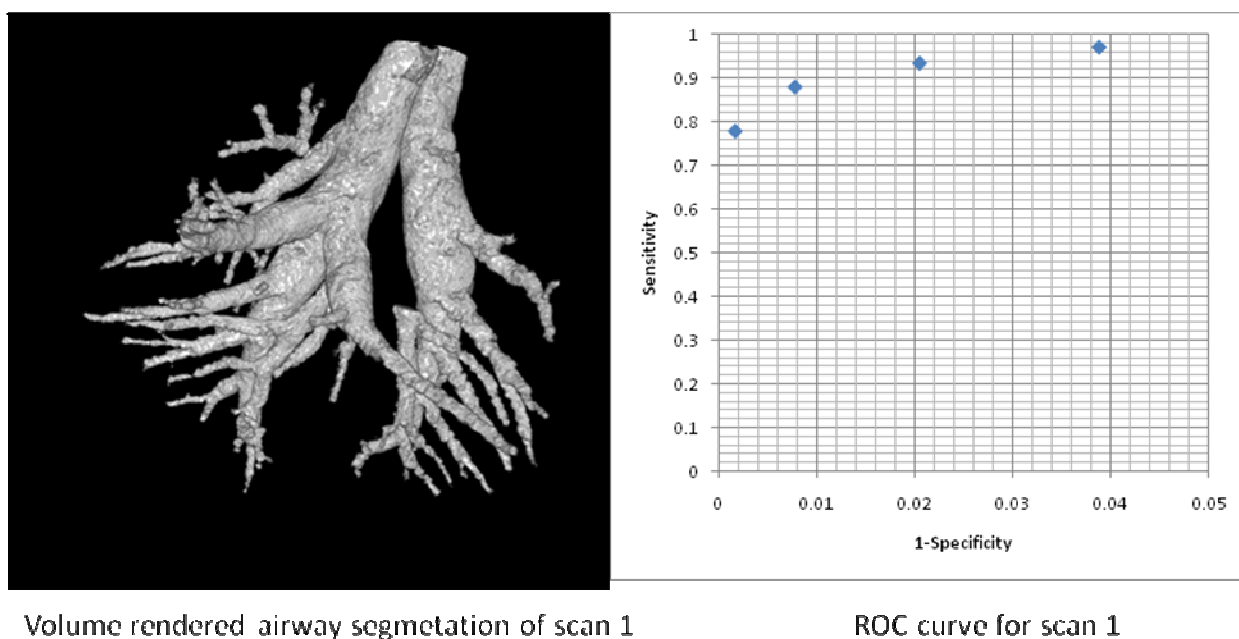
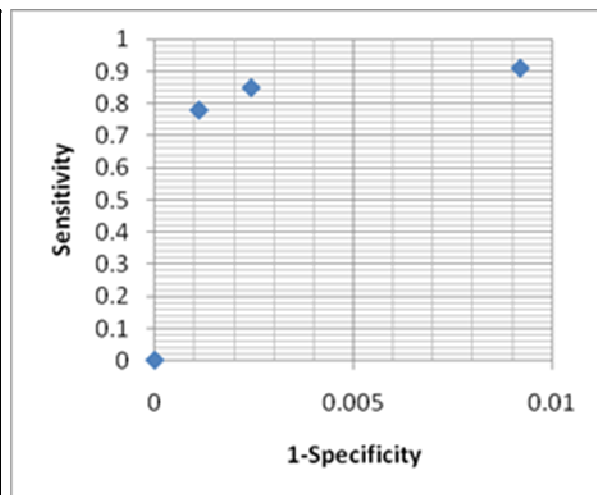


Figure 17 - continued



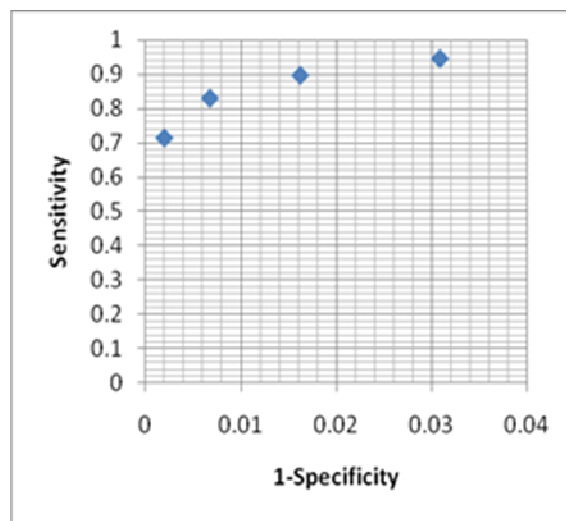
Volume rendered airway segmentation of scan 2



ROC curve for scan 2



Volume rendered airway segmentation of scan 3



ROC curve for scan 3

Figure 17. Volume rendered airway segmentation for three different scans

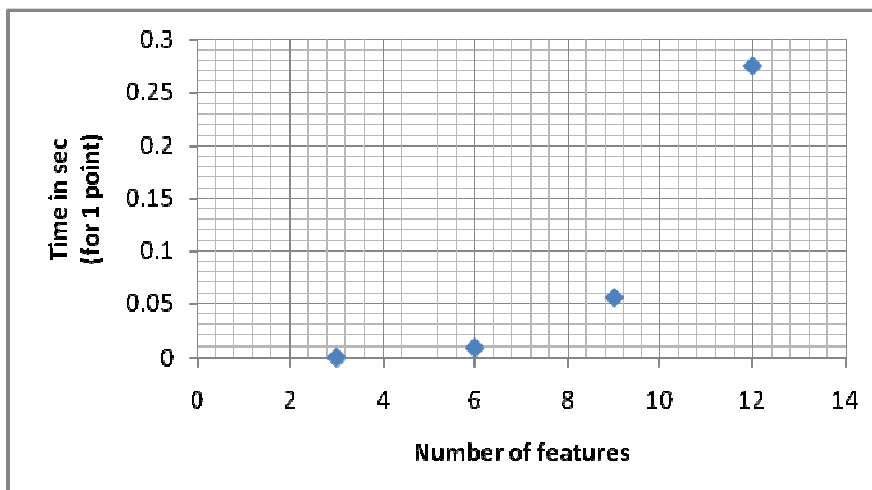


Figure 18. Graph showing the increase in time per query point with the increase in the number of features (increase in dimension of feature space)

It was observed that ANN took about 0.0015 sec per point for the KNN-classification in a 12 dimensional space which is permissible when compared to the STANN's performance of 0.275 sec per query point. The use of ANN is the one that is most suitable for classifying the points of this type of image.

In order to optimize the time of classification for millions of query points based on the training data set, an error bound parameter EPS developed in the ANN library was changed from 0 (for exact computation) to 1 (for approximate computation). The test was performed to check for the correctness as well as the reduction in the computation time when an error bound limit is accepted with respect to computing the distances. A significant reduction in the classification time of a single query data set was observed which has been shown in figure 19.

The decrease in the computation time by accepting an error bound KNN classification did not affect the specificity and sensitivity values greatly. Figure 20 illustrates the change in the sensitivity and specificity values compared with the exact classification by setting the EPS to 0.

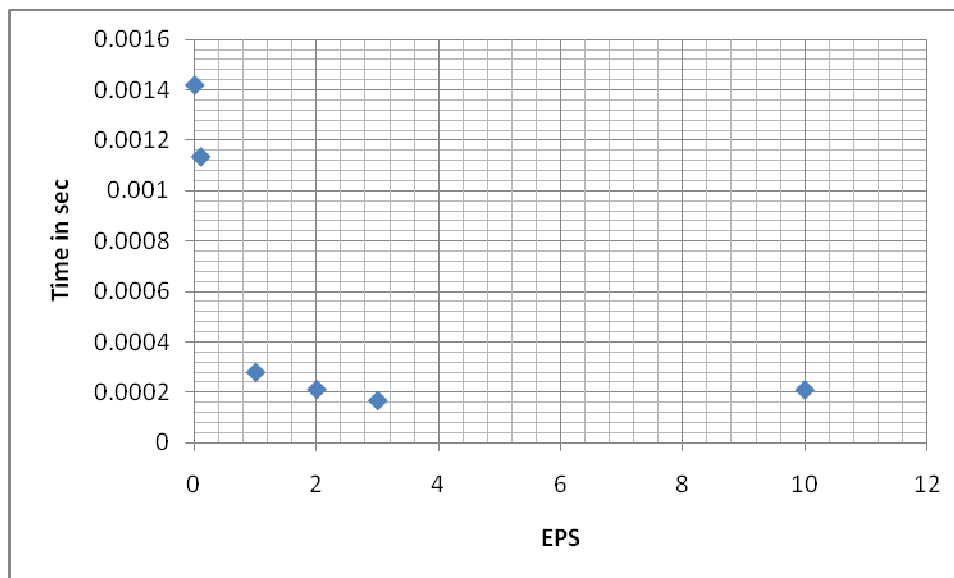


Figure 19. Graph showing the reduction in the time for classification of all the voxels in a query image by increasing the error bound limits

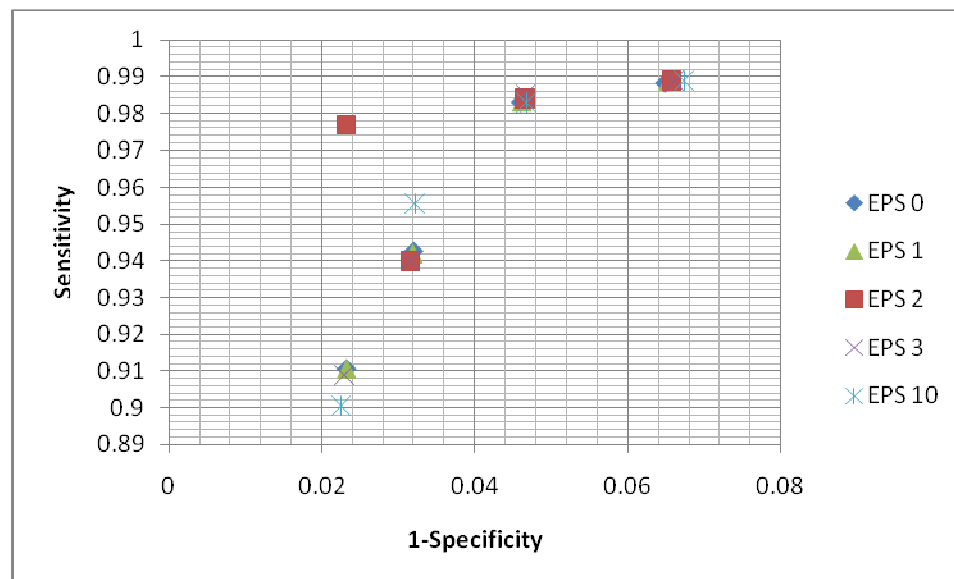


Figure 20. Graph showing the change in the ROC curve with the changing error bound limits.



## CHAPTER 5

### DISCUSSION

#### 5.1 Advantages of the proposed method

The method proposed in this thesis has several advantages compared to the previous methods. Unlike the previous in-vivo mice airway segmentation methods (based on image intensities), the current algorithm helps to overcome the difficulty of segmenting the airways in scans with minimal contrast between airways and vasculature. Thus airway segmentation from an excised mouse lung which provides greater detail and information about the airways is one of the major departures of this method from the previous methods of segmenting airways from an in-vivo scan (as described in section 2.6). Also, this algorithm has reduced the required time for segmenting and analyzing the airways from one week to three hours. This reduction in time offers a potential for faster clinical diagnosis of abnormalities and for quicker drug trials.

Compared to the previous work done by Shi [10] (dependent only on the grayscale morphology of the scan) and Artaechevarria [11] (dependent on the wave front propagation) on the automatic in-vivo mice airway segmentation, the current algorithm mainly relies on the voxel probabilities of an image calculated using texture, shape and appearance features. This ensures the segmentation results to be based on the information (as per section 4.1) of the structure to be segmented rather than relying on the imaging intensities of the scan provided by the scanner. In the work by Shi, there was a problem of detecting the in-plane branches and extra-computation complexity of 2D segmentation to 3D volume reconstruction. Also, in the work by Artaechevarria, noise or disease interruptions in the airway branch would stop the further segmentation. The current algorithm considers the above problems and achieves segmentation results by computing

a 3D segmentation volume using noise removal and structure enhancement features in classification.

As we know, in pattern recognition techniques, the data is classified for assigning a given piece of input data into one of a given number of categories. There are many classifiers like the maximum entropy classifiers, Naive Bayes classifiers, support vector machines, decision trees, radial basis function and k-nearest neighbor classifiers.

However, the current research has been built on a previously published framework of airway tree segmentation by K nearest neighbor classification [12]. This previous work done by Lo et al. was implemented to classify only the terminal branches of the human airway tree. Unlike the current method of classifying all the voxels of the airway region, the bigger branches (Trachea and Main bronchi) in the previous method were segmented using region growing. Another major difference of the previous method was in the selection of an optimum threshold (for final region growing segmentation) from the ROC curve during the selection of best features step. In the current algorithm, the probability image is segmented over four equally spaced threshold ranges.

Another advantage of this algorithm is that it automatically segments the airways in mice lung with minimal human intervention. A commercial image based software diagnostic tool, helps in determining the measurements of the airway geometry and airway reactivity with the help of the segmentation generated by the current algorithm.

## 5.2 Factors influencing the results

There are a few leakages at places along the airway tree where there is a very thin or negligible wall present between the airway and the vasculature. This is mainly caused due to the poor resolution of the micro-CT scans which show the wall between the airways and vessels with minimal contrast. In such cases, the algorithm detects the

vessels as a part of the airway which is equally hard to distinguish with the naked eye. An example of such a case is as shown in figure 21 and figure 22.

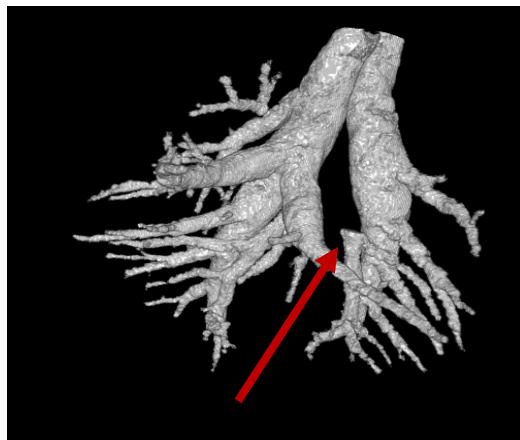


Figure 21. Volume rendering of an incorrectly segmented vessel running parallel to the airway wall, red arrow shows the vessel Vessel which is parallel to the airway walls is segmented

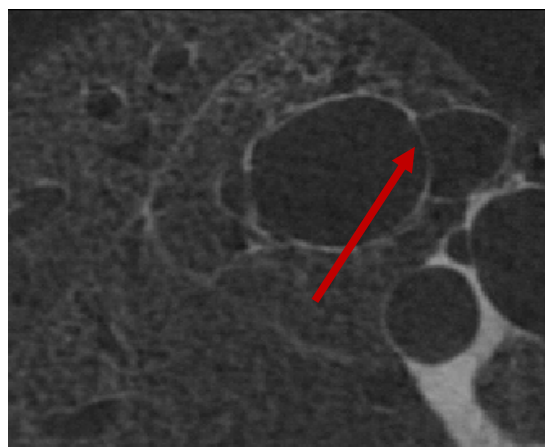


Figure 22. Midslice of the scan showing the wall between the airway and the vessel.

Another factor that greatly determines the results of the segmentation is the selection of the threshold for region growing using connected threshold algorithm. This is mostly in the range of 0.8 to 0.9 for the probability image but might vary a little for some images. In cases where this threshold is not appropriate for a scan, it might result in a leakage or detection of incorrect region as airways. Different values for the threshold may be tried in the above range in order to achieve accurate segmentation. The example is as shown in figure 23.

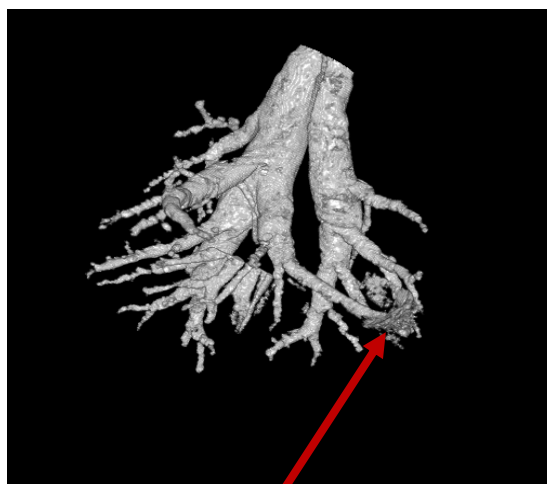


Figure 23. Misclassification/Leakage of airways due to the incorrect threshold selection by the user

For segmentation of airways in the scans with different resolution, quality and structures in the airway tree, the classifier should be trained again. This is because the features that show good performance on a set of training data during the training phase are bound to show similar behavior with other scans from the similar set.

## CHAPTER 6

### CONCLUSION

The voxel classifier presented in this paper offers an automatic tool to perform ex-vivo mice airway tree segmentation from a lung volume micro-CT image. The research presented in this thesis enables us to detect any abnormalities in the airways. This is made possible by the algorithm that has been developed to measure the physical dimensions of the segmented airways. The algorithm is developed based on voxel based classification of an airway structure (unlike the traditional region growing based algorithms) that improves the scope for the detection of many branches which are missed by traditional methods. Compared to manual segmentation, the segmentation results of the three micro-CT images indicate nearly 80% accuracy in airway detection based on the sensitivity and specificity values. The time required to process each scan has also been drastically decreased with the help of the proposed algorithm. This makes it possible to analyze a much larger number of scans for the study of longitudinal or drug-responsive behavior of airways.

## REFERENCES

- [1] Chronic Obstructive Pulmonary Disease International. COPD statistical information <http://www.copd-international.com/library/statistics.htm> (accessed Jun 9, 2010).
- [2] American Academy of Allergy Asthma and Immunology. Asthma Statistics <http://www.aaaai.org/media/statistics/asthma-statistics.asp> (accessed May 30, 2010)
- [3] Deniz Aykac, Eric A. Hoffman, Geoffrey McLennan, and Joseph M. Reinhardt, "Segmentation and Analysis of the Human Airway Tree from Three-Dimensional X-Ray CT Images," IEEE Transactions on Medical Imaging, vol. 22, no. 8, August 2003.
- [4] C.G. Irvin and J.H. Bates, "Measuring the lung function in the mouse: the challenge of size," *Respir Res*, vol.4, pp. 4, 2003.
- [5] J. B. West. 2005. *Respiratory Physiology: The Essentials*, Seventh ed., Lippincott Williams and Wilkins.
- [6] International database resource for laboratory mouse. The Jackson Laboratory. "Mouse Genome Informatics", vol. 2007, 2007. <http://www.informatics.jax.org/> (accessed July 2, 2010)
- [7] B. R. Wallau, A. Schmitz, and S. F. Perry, "Lung morphology in rodents (Mammalia, Rodentia) and its implications for systematic," *J. Morphol*, vol. 246, pp. 228-48, 2000.
- [8] J. Tshchirren, E.A. Hoffman, G. McLennan, and M. Sonka, "Intrathoracic airway trees: segmentation and airway morphology analysis from low-dose CT scans," *IEEE Trans Med Imaging*, vol. 24, pp.1529-39, 2005. Wonkyu Park, Eric A. Hoffman, and Milan Sonka, "Segmentation of Intrathoracic Airway Trees:A Fuzzy Logic Approach", *IEEE Trans Med Imaging*, vol 17, August 1998.
- [9] Kai Lai, Peng Zhao, Yufeng Huang, Junwei Liu, Chang Wang, Huanqing Feng, "Automatic 3D Segmentation of Lung Airway Tree: A Novel Adaptive Region Growing Approach," *IEEE Explore*, 2009.
- [10] L.Shi, J. Thiesse, G. McLennan, E.A. Hoffman, and J.M. Reinhardt, "Three dimensional murine airway segmentation in micro-CT images", presented at SPIE Medical Imaging, San Diego, CA, 2007.
- [11] X Artaechevarria, D P´erez-Mart´ın, M Ceresa, G de Biurrun, D Blanco, L M Montuenga, B van Ginneken, C Ortiz-de-Solorzano and A Mu˜noz-Barrutia, "Airway segmentation and analysis for the study of mouse models of lung disease using micro-CT", *Phys. Med. Biol.* 54 (2009) 7009–7024
- [12] Penchin Lo, Jon Sparring, Haseem Ashraf, Jesper J.H. Pedersen and Marleen de Bruijne, "Vessel-guided airway tree segmentation: A voxel classification approach", *Medical Image Analysis* 14 (2010) 527-538.

[13] David M. Mount and Sunil Arya, “ANN Programming library”, ANN, Version 1.1.2, Released 27 Jan 2010, <http://www.cs.umd.edu/~mount/ANN/>

[14] Insight Tool Kit software guide, Second edition, Updated for ITK version 2.4. <http://www.itk.org/ItkSoftwareGuide.pdf>

[15] Kristian Sanberg, “Visualizing Calculus – The use of the gradient in image processing”. <http://amath.colorado.edu/outreach/demos/hshi/2001Spr/snake/snake.html>

[16] Per-Erik Danielsson. Analysis of 3D-volume data using 2nd derivatives. In Proceedings DICTA-95, pages 14{19, St John's College, University of Queensland, Brisbane, December 1995.

[17] Jiri Hladuvka, Andreas Konig, and Eduard Groller , “ Exploiting Eigenvalues of the Hessian Matrix for Volume Decimation”, Title of the page as listed on the website. <http://www.cg.tuwien.ac.at/research/vis/vismed/evDecimation/evDecimation.pdf>

[18] A.F. Frangi, W.J. Niessen, K.L. Vincken, M.A. Viergever (1998). Multiscale vessel enhancement filtering. In Medical Image Computing and Computer-Assisted Intervention - MICCAI'98, W.M. Wells, A. Colchester and S.L. Delp (Eds.), Lecture Notes in Computer Science, vol. 1496 - Springer Verlag, Berlin, Germany, pp. 130-137.

[19] P. Pudil, F.J. Ferri, J.Novovicova and J.Kittler, “ Floating Search Methods for Feature Selection with Nonmonotonic Criterion Functions”, 1051-4651/94, IEEE, 1994.

[20] Rafael Wiemker, Thomas Bülow and Thomas Blaffert, “Unsupervised extraction of the pulmonary interlobar fissures from high resolution thoracic CT data”, International Congress Series 1281 (2005) 1121 – 1126

[21] Simon Warfield, “Fast  $k$ -NN classification for multichannel image data”, Elsevier, Pattern Recognition Letters, Volume 17, Issue 7, 10 June 1996, Pages 713-721

[22] Michael Connor, Piyush Kumar, “Fast construction of  $k$ -Nearest Neighbor Graphs for Point Clouds”, IEEE transactions on visualization and computer graphics, September 2009. <http://compgeom.com/~stann>.

[23] Marco Loog, Bram van Ginneken, “Supervised Segmentation by Iterated Contextual Pixel Classification”, icpr, vol.2, pp.20925, 16<sup>th</sup> International Conference on Pattern Recognition (ICPR'02) – Volume 2, 2002.

[24] Michael B. Merickel Jr., Michael D. Abramoff, Milan Sonka, Xiaodong Wu, “Segmentation of the Optic Nerve Head Combining Pixel Classification and Graph Search”, Proc SPIE, pp.651215-10 2007.

[25] Xiayu Xu. 2010. “Simultaneous automatic detection of optic disc and fovea.” MS diss., University of Iowa.

[26] D.F.Malan, C.P. Botha, R.G.H.H. Nelissen, E.R. Valstar, “Voxel classification of periprosthetic tissues in clinical computed tomography of loosened hip prostheses”, IEEE 978-1-4244-4126-6/10.

[27] Jacqueline Thiesse Namati, 2009, “Phenotype characterization of lung structure in inbred mouse strains using multi modal imaging techniques.”, PhD diss., University of Iowa

[28] Besaratinia A, Pfeifer GP, “Applications of the human p53 knock-in (Hupki) mouse model for human carcinogen testing”, FASEB J. 2010 Aug;24(8):2612-9. Epub 2010 Apr 6.



## APPENDIX

The implementation details of the scales and type of feature images calculated as per section 3.1 is described here with the help of following tables. The representation of a feature image has two coordinates, the first coordinate represents the scale number of the feature image and the second coordinate represents the type/feature number of the feature image. For example, for the feature image represented in the algorithm with coordinates (5,11), the first coordinate from the scale table represents the scale value (5 means scale value = 2 ) and the second coordinate represents the type of feature (11 means scale type = Eigen value of Hessian Image 1). This representation is useful only to ease the implementation and naming of the set of 147 features. The coordinates are the number representation of the scale and type which can be decoded using the following tables.

Scale Number	Scale/Standard Deviation
0	0.01
1	0.05
2	0.1
3	0.5
4	1
5	2
6	3

Table A1. Representation of the scale with the corresponding scale numbers

Feature Number	Feature Name
0	Gaussian Image
1	First Order Derivative in X direction
2	First Order Derivative in Y direction
3	First Order Derivative in Z direction
4	Second Order Derivative with respect to ZZ direction
5	Second Order Derivative with respect to YY direction
6	Second Order Derivative with respect to XX direction
7	Second Order Derivative with respect to YZ direction
8	Second Order Derivative with respect to XZ direction
9	Second Order Derivative with respect to XY direction
10	Gradient Magnitude Image
11	Eigen Value of Hessian Image 1
12	Eigen Value of Hessian Image 2
13	Eigen Value of Hessian Image 3
14	Laplacian Image
15	Gaussian Curvature Image
17	Eigen Ratio Image 1 - $(\text{HessianImage2}/\text{HessianImage1})$
18	Eigen Ratio Image 2 - $(\text{HessianImage3}/\text{HessianImage1})$
19	Eigen Ratio Image 3 - $((\text{HessianImage1} \times \text{HessianImage2})/(\text{HessianImage1} + \text{HessianImage2}))$

Table A2. Representation of the feature types with their corresponding feature numbers